FINAL TECHNICAL REPORT

Cooperative Agreement NCC 2-1148

"Evolution of the Earth and Origin of Life: The Role of Gas/Fluid Interactions with Rocks"

Friedemann Freund, Principal Investigator

Period of Performance
December 1, 1999 to May 31, 2001

Submitted by:
The Center for the Study of Life In The Universe
SETI Institute
2035 Landings Drive
Mountain View, CA 94043
650-961-6633

Date Submitted:
10/30/2001

CASI

Evolution of the Earth, and Origin of Life: Gas/Fluid Interactions with Rocks

Abstract

The work under the Cooperative Agreement will be centered on questions of the evolution of Life on the early Earth and possibly on Mars. It is still hotly debated whether the essential organic molecules were delivered to the early Earth from space (by comets, meteorites or interplanetary dust particles) or were generated *in situ* on Earth. Prior work that has shown that the matrix of igneous minerals is a medium in which progenitors of organic molecules assemble from H_2O, CO_2 and N_2 incorporated as minority "impurities" in minerals of igneous rocks during crystallization from $H_2O/CO_2/N_2$–laden magmas. The underlying processes involve a redox conversion whereby C, H, and N become chemically reduced, while O becomes oxidized to the peroxy state. During Year 02 the work will be divided into three tasks. Task 1: After carboxylic (fatty) acids and N-bearing compounds have been identified, other extractable organic molecules including lipids, oily substances and amino acids will be studied. Dedicated lipid analysis will be combined with gas chromatographic-mass spectroscopic (GC-MS) analysis of organic compounds extracted from minerals and rocks. Task 2: Using infrared (IR) spectroscopy, C-H entities that are indicators for the organic progenitors in mineral matrices will be studied. A preliminary heating experiment with MgO single crystals has shown that the C-H entities can be pyrolyzed, causing the IR bands to disappear, but at room temperature the IR bands reappear in a matter of days to weeks. This work will be expanded, both by studying synthetic MgO crystals and olivine crystals from the Earth's upper mantle. The C-H bands will be compared to the published "organic" IR feature of dust in the interstellar medium (ISM) and interplanetary dust particles (IDP). Task 3: A paradox marks the evolution of early Life: Oxygen is highly toxic to primitive life, yet early organisms "learned" to detoxify *reactive oxygen species*, to utilize oxygen, and even produce it. Why would organisms on the early anaerobic Earth be under evolutionary pressure to evolve defenses against *reactive oxygen species*? Minerals in igneous rocks are now known to contain peroxy. When such minerals weather, the peroxy hydrolyzes to H_2O_2. The hypothesis will be tested whether organisms living in intimate contact with rock surfaces are subjected to a constant trickle of H_2O_2 and thus under stress to develop strategies to either detoxify the *reactive oxygen species* or repair the molecular damage that they cause. Understanding these processes is central to the Astrobiology mission. It opens new avenues toward understanding the evolution of early life on Earth, and the potential for aerobic life elsewhere. This Cooperative Agreement also has a strong educational and public outreach component involving high school, undergraduate students, and high school teachers.

Outline

Understanding the origins of Life requires a good understanding of the physics and chemistry of biogenic low-z elements H, C, N, O, P, S in all kinds of environments, terrestrial, on Mars, on other extraterrestrial bodies such as meteorite parent bodies and comets, and in interstellar space. The work presented here aims at elucidating aspects of low-z element geo- and cosmochemistry with reference to the origin of Life on Earth and to the search for life on Mars, extant or extinct. The main thrust of the work is concerned with the formation of organic molecules such as oxygenated H-C-N-O molecules or precursors thereof inside the matrix of igneous and high-grade metamorphic minerals, and the presence of peroxy and of H_2 in rocks.

The formation of complex organic molecules inside the "hard" matrix of structurally dense magmatic minerals, in particular, oxygenated H–C–O molecules or precursors of the general composition $H_XC_YO_Z^{n-}$, occurs through a series of reactions in the solid state, beginning with the dissolution of H_2O and CO_2 in magmatic minerals during their crystallization from an H_2O/CO_2

saturated melt, proceeding with a redox conversion of solute H_2O and CO_2 into H_2 plus reduced C, and the formation of $H_xC_yO_z^{n-}$ precursors through segregation of H_2 and C into dislocations and other major defects, and ending with the release of H–C–O molecules through the weathering process. Evidence for $H_xC_yO_z^{n-}$ precursors has been obtained through extraction of crushed synthetic MgO and olivine single crystals from the upper mantle [refs]. The analytical tools employed include infrared (IR), thin layer chromatography (TLC), nuclear magnetic resonance (^{1}H-NMR, ^{13}C-NMR) spectroscopy, and gas chromatography -mass spectroscopy (GC-MS).

It has been shown that oxygen in its common 2– oxidation state acts as the electron donor in the above-mentioned redox conversion of solute H_2O and CO_2 [refs]. In the process oxygen changes from O^{2-} O^-, forming peroxy entities in the mineral structures. The peroxy dissociation generates electronic charge carriers, also known as positive holes, equivalent to defect electrons in the oxide anion sublattice, which are highly mobile electronic charge carriers.

If rocks contain peroxy, they must also contain H_2 as a by-product of the above-mentioned redox conversion. Using ultrasensitive GC detection techniques, the release of H_2 during fracture will be studied. If rocks contain peroxy but have lost H_2, they will release oxygen during weathering through the intermediate of hydrogen peroxide formation, H_2O_2. Assuming that the Earth had an active weathering cycle after the formation of the first continents, this process should lead to a slow but inextricable oxidation of the entire planet, its ocean and its atmosphere. Likewise, if rocks contain peroxy, the H_2O_2 formed during weathering might have represented a formidable challenge to early microbial organisms that lived in intimate contact with rocks.

The results obtained as part of the work conducted under this Cooperative Agreement are described in the following publications and conference papers.

Proc. Natl. Acad. Sci. 98: 2142-2147 (2001)

Organic Protomolecule Assembly in Igneous Minerals

Friedemann Freund[1], Aaron Staple[2], and John Scoville[3]

[1] SETI Institute/NASA Ames Research Center
[2] Stanford University
[3] University of Kentucky

Abstract

C–H stretching bands, ν_{CH}, in the infrared spectrum of single crystals of nominally high purity, laboratory-grown MgO and of natural upper mantle olivine provide an "organic" signature that closely resembles the symmetrical and asymmetrical C–H stretching modes of aliphatic $-CH_2-$ units. The ν_{CH} bands indicate that H_2O and CO_2, dissolved in the matrix of these minerals, converted to form H_2 and chemically reduced C, which in turn formed C–H entities, probably through segregation into defects such as dislocations. Heating causes the C–H bonds to pyrolyze and the ν_{CH} bands to disappear, but annealing at 70°C causes them to reappear within a few days or weeks. Modeling dislocations in MgO suggests that the segregation of C can lead to C_x chains, $x \leq 4$, with the terminal C atoms anchored to the MgO matrix by bonding to two O^-. Allowing H_2 to react with such C_x chains leads to $[O_2C(CH_2)_2CO_2]$ or similar precipitates. It is suggested that such C_x–H_y–O_z entities represent protomolecules from which derive the short-chain carboxylic and dicarboxylic and of the medium-chain fatty acids that have been solvent-extracted from crushed MgO and olivine single crystals, respectively. Thus it appears that the hard, dense matrix of igneous minerals represents a medium in which protomolecular units can be assembled. During weathering of rocks the protomolecular units turn into complex organic molecules. These processes may have provided stereochemically constrained organics to the early Earth that were crucial to the emergence of Life.

[1] Corresponding author:
Friedemann Freund
SETI Institute/NASA Ames Research Center
MS 239-15
MOFFETT FIELD, CA 94035-1000
Tel. 650 604-5183
Fax 650 604-1092
e-mail ffreund@mail.arc.nasa.gov

Introduction

Of all natural environments where chemical reactions occur that produce organic molecules, the dense hard matrix of igneous minerals may appear as the most unlikely place. Yet, our earlier research has shown that a suite of medium-to-long chain fatty acids, C_6- C_{12}, can be identified among the organics extracted from crushed olivine single crystals from the $CO/CO_2/H_2O$–laden high temperature, high pressure environment of the upper mantle (1). Freshly crushed olivine single crystals, when heated in vacuum, were found to release a range of organic molecules, including aromatic compounds (2). Solvent extraction of crushed MgO crystals, grown in the laboratory at 1 bar from a $CO/CO_2/H_2O$–saturated MgO melt (3), produced short-chain carboxylic and dicarboxylic acids up to C_4 (4).

When minerals grow either in the laboratory or in nature, their environments are always "contaminated" and often saturated with CO_2 and H_2O. The presence of CO_2 and H_2O introduces the low-z elements carbon and hydrogen as "impurities" into the mineral matrix. As will be shown in this report, solute C and H_2 participate in reactions that lead to the precipitation of protomolecular C_x entities and formation of C-H bonds inside the hard, dense mineral matrix. These solid state reactions are different from the reactions that lead to the synthesis of lipids under hydrothermal conditions by Fischer-Tropsch-type reactions (5) or to the reduction of CO_2 during serpentinization of olivine and the production of organics with the help of catalysts such as magnetite (6) or to any other abiogenic reaction that has been considered for the early Earth (7-9).

Dissolution of H_2O and CO_2 in Mineral Matrices

H_2O becomes incorporated into the matrix of minerals that crystallize in H_2O–laden environments, even of minerals that are nominally anhydrous. The basic reaction controlling the uptake of "impurity" H_2O can be described as a proton transfer from H_2O onto an O^{2-} of the host oxide/silicate matrix:

$$H_2O + O^{2-} = 2\ OH^- \qquad [1]$$

A large body of literature exists about OH^- in nominally anhydrous minerals from various geological settings (10, 11). The most widely employed method of analysis is infrared (IR) spectroscopy. If transparent crystals are available, IR can detect very small amounts of OH^- by way of their O-H stretching bands, ν_{OH}, in the range of 3000-3700 cm^{-1}. Because the ν_{OH} bands lie at relatively high wavenumbers and are decoupled from the lower frequency lattice modes, they are generally sharp and unambiguously identifiable.

The amounts of OH^- in olivine, $(Mg,Fe)_2SiO_4$, the dominant upper mantle mineral, range from 10-1000 $H/10^6$ Si (ppm) (11). Similar but generally low OH^- concentrations have been found in other petrologically important minerals (10). Under the assumption that eq. [1] completely describes the dissolution reaction of H_2O, the OH^- concentrations determined by IR have been used to calculate the total amount of chemically bound "water".

CO_2 is the dominant gas in many volcanoes and the dominant gas/fluid component in the magmas that feed them. The important role that CO_2 plays in the petrogenesis of igneous rocks has also long been recognized. At high pressures it can lower the melting points of mineral assemblies, i.e. the temperatures at which partial melts form, by hundreds of degrees (12). While CO_2 is known to dissolve in quenched high-pressure silicate melts, maybe in form of carbonate anions, CO_3^{2-}, (13, 14), some researchers maintain that C or CO_2 will not enter as "impurity" into the solid matrix of minerals (15, 16). The formation of a carbonate anion can be described as the merging of a CO_2 molecule with a lattice O^{2-} without changing the oxidation state of the carbon:

$$CO_2 + O^{2-} = CO_3^{2-} \qquad [2]$$

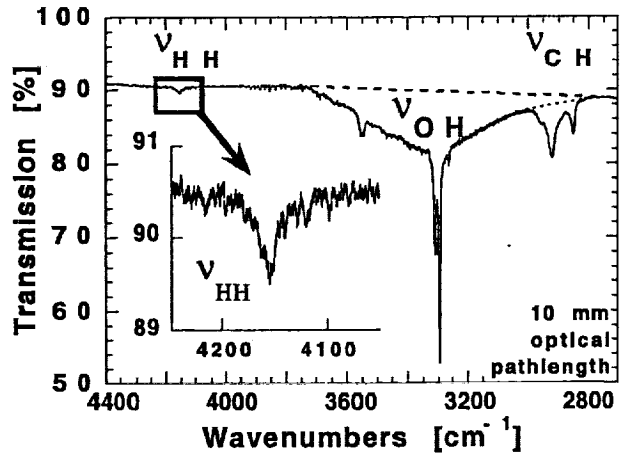

Figure 1: Infrared spectrum of a nominally high purity MgO crystal, grown from a $CO/CO_2/H_2O$–laden melt, in the 2800-4200 cm^{-1} range covering the H-H, O-H and C-H stretching frequencies.

At closer inspection dissolution of H_2O and CO_2 in solid matrix turns out to be more complicated than eqs. [1] and [2] might suggest. This is exemplified by **Figure 1** which displays the IR spectrum of a nominally high purity MgO single crystal*, grown from an MgO melt equilibrated with an atmosphere of CO/CO_2 plus H_2O and N_2 at 1 bar pressure (3). In the center a group of ν_{OH} bands is seen that consists of (i) a relatively strong band or group of bands around 3300 cm^{-1}, (ii) a weaker band at 3560 cm^{-1}, and (iii) a very broad band extending from below 3000 cm^{-1} to 3700 cm^{-1}. Because MgO crystallizes in the simple, face-centered cubic rocksalt structure, the ν_{OH} bands (i)-(iii) have been assigned to single OH^- adjacent to an Mg^{2+} vacancy site, to OH^- pairs adjacent to an Mg^{2+} vacancy site, and to interstitial OH^-, i.e. H^+ associated with O^{2-} at regular O^{2-} sites, respectively (17).

Figure 1 also shows a weak but distinct band on the left, at 4152 cm^{-1} (enlarged in the inset). It has the characteristic signature of a ν_{HH} band arising from the H-H stretching mode of lattice-bound H_2 molecules similar to the ν_{HH} band of H_2 in noble gas matrices (18). Since the ν_{HH} band is intrinsically weak, the fact that it can be observed in the MgO crystal under study suggests a high concentration of H_2 molecules.

This ν_{HH} band and the ν_{CH} bands on the right of **Figure 1**, between 2800–3000 cm^{-1}, jointly point at the complexity of the solid state dissolution of H_2O and CO_2. The ν_{CH} bands suggest that some form of C–H entities formed in the MgO crystal, providing an "organic" signature. These C–H entities do not come from surface contamination as has been suggested (16, 19, 20) but are associated with C in the bulk that remains detectable even upon heating in ultrahigh vacuum up to 700-900°C (21-23).

The main focus of this study will be to address the nature this "organic" signature and how the presence of C–H entities is linked to the dissolution mechanism of H_2O and CO_2 in mineral matrices.

Experimental Procedures

* Nominal high purity refers to metal cation impurities only, which are routinely measured. It does not take into account impurities that may arise from the dissolution of gases in solid matrix.

We chose MgO crystals for the basic study because MgO crystallizes in the simple, face-centered cubic rocksalt-type (NaCl) structure, consisting of a close packing of O^{2-} anions with the Mg^{2+} cations occupying all available octahedral sites. A further advantage of MgO is that large single crystals can be grown from the melt in high purity grades. The structure of olivine, $(Mg,Fe)_2SiO_4$, though orthorhombic, is similarly dense, deriving from a hexagonal close packing of O^{2-} anions with Mg^{2+} and Fe^{2+} cations in two differently distorted octahedral sites and Si^{4+} in tetrahedral sites. Both, MgO and olivine, tend not to develop internal cleavage planes as some other minerals do, in particular pyroxenes.

The MgO crystals used in this study were grown at 1 bar pressure from a $CO/CO_2/H_2O$–saturated melt (3). Nominally, i.e. with respect to metal impurities, these MgO crystals were of 99.9% purity, colorless, with some turbidity due to μm and sub-μm sized cavities that decorate a dense network of subgrain boundaries and dislocations. They were available in form of large cubes, 20-30 mm in size, reflecting the perfect cleavage of MgO along (100). The olivine single crystals used in this study came from Afghanistan. They were recovered from peridotite nodules brought up by volcanic eruptions (24). The crystals were 20-30 mm in size, irregular in shape, olive-green and partly turbid due to a decorated network of subgrain boundaries and dislocations. A selected large olivine crystal was cut with a low-speed diamond saw to a rectangular shape of about 20 x 10 x 6 mm. This olivine crystal and a similarly sized MgO crystal were cut into several identical pieces, about 5 x 10 x 6 mm, so that the study to be described below could be done with pieces of the same single crystals. The cut surfaces were left "as is", i.e. without further grinding or polishing.

The single crystal pieces were cleaned with organic solvents. They were mounted in Al blocks that fit into the sample holder of the Nicolet Nexus 670 FT-IR spectrometer. The MgO and olivine crystals were heated for 12 hrs to 400°C and 45 min to 300°C in a stream of high purity N_2 gas, respectively. Previously it had been shown by gas chromatographic techniques (1, 4) that, after drying, no solvents are retained, even on finely crushed single crystal powders. By measuring the ν_{CH} intensities from a thick MgO crystal and then cutting the same crystal into several slices it had been shown earlier (17) that the ν_{CH} band strength correlates with the length of the optical path through the bulk, not with the number of surfaces, indicating that the signal came from C-H entities in the bulk. All IR spectra (before and after heating) were recorded at 30°C, acquiring data during 20 scans over the range 400-4000 cm^{-1}.

The heat treatment pyrolyzed their C-H entities in the MgO and olivine crystals, causing their ν_{CH} bands to disappear or nearly disappear as determined from the IR spectra recorded immediately after cooling to room temperature. For the next 32 days sets of these MgO and olivine crystals (wrapped in Al foil) were stored in air at 70°C, while one control set was stored at 24°C. A run started at 45°C was lost due to a malfunction of the temperature controller. The IR spectra of each sample were recorded, first in daily intervals, later in weekly intervals. In the case of MgO the background in the ν_{CH} region was fitted linearly between 2785 cm^{-1} and 3025 cm^{-1}. In the case of olivine a best-fit polynomial was used to compensate for the more steeply sloping background.

Dislocations in MgO were modeled using the CrystalMaker 4.0 program by David C. Palmer modified in such a way as to allow the introduction of defects into the perfect structure. No lattice relaxation around the dislocation cores was taken into account.

Results

Figure 2 shows the $\_{CH}$ bands in the "as received" MgO and olivine crystals, i.e. prior to heating. In both cases the bands are similar in number and with respect to their position and relative intensities. The two strongest $\_{CH}$ bands lie at 2926 and 2855 cm^{-1} in MgO and at 2922 and 2852 cm^{-1} in olivine.

Minor bands occur at 2955 and 2870 and a shoulder at 2895 cm^{-1}. MgO exhibits an additional weak band at 3008 cm^{-1}, which the spectrum of olivine does not show. In MgO all ν_{CH} bands are slightly broader than in olivine.

The different ν_{CH} bands may arise from C-H entities in different local environments or from C_x entities in which some C atoms are bonded to two or more H, thereby giving rise to a set of symmetrical and asymmetrical C-H stretching modes. Indeed, the two strongest bands at 2926 and 2855 cm^{-1} in MgO and at 2922 and 2852 cm^{-1} in olivine agree with the symmetrical and asymmetrical C-H stretching modes of $-CH_2-$ units in aliphatic hydrocarbon chains such as in polyethylene (25). The weak band at 2955 cm^{-1} and a companion at 2870 cm^{-1} agree with the symmetrical and asymmetrical C-H stretching modes of $-CH_3$ units.

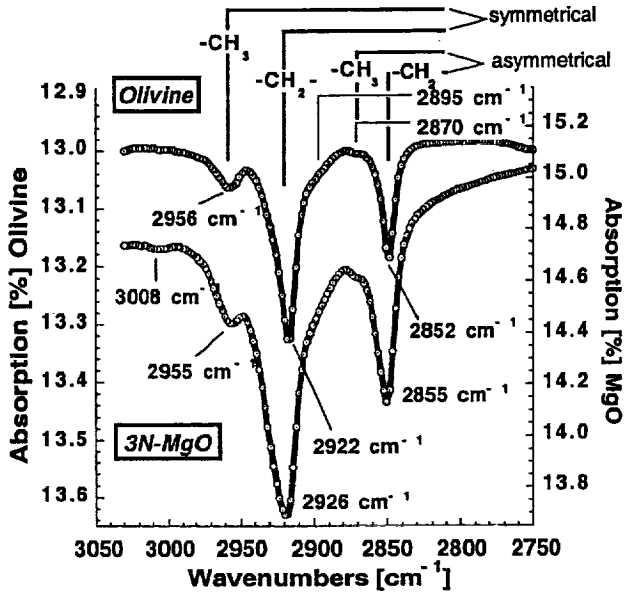

Figure 2: C-H stretching bands, ν_{CH}, in the synthetic MgO and an upper mantle derived olivine single crystal recorded prior to heating. The strongest ν_{CH} bands appear to arise from symmetrical and asymmetrical C-H stretching modes of $-CH_2-$ entities with minor ν_{CH} bands probably due to $-CH_3$. The ν_{CH} bands of MgO are broader than those of olivine.

The weakness of the ν_{CH} signature does not necessarily mean that the amount of solute C_x entities is small. The strength of the ν_{CH} bands solely depends on the number of C–H bonds formed, not on the number of C atoms in the C_x entities. The total C concentration in the laboratory-grown MgO single crystals is probably of the order of 50-100 ppm (21, 26). Similar total C concentrations have been reported for upper mantle-derived olivine crystals (27, 28), and at least 5 ppm C_2- C_6 hydrocarbons.

Heating the MgO crystal to 400°C and the olivine crystal to 350°C caused their ν_{CH} bands to nearly completely disappear, due to *in situ* pyrolysis of the C–H bonds. **Figure 3** shows how the ν_{CH} bands reappear in the MgO crystal during annealing at 70°C. The band positions are slightly shifted. At the end of 32 days at 70°C the integral intensity of the ν_{CH} bands reached about 10% of the initial intensity. Annealing at 95°C and 24°C caused the ν_{CH} bands to reappear faster and slower, respectively. The new ν_{CH} bands lie at nearly the same positions as the ones observed before heating.

This suggests that, while heating pyrolyzed the C–H bonds, it left the C_x entities intact to which the H atoms had bonded.

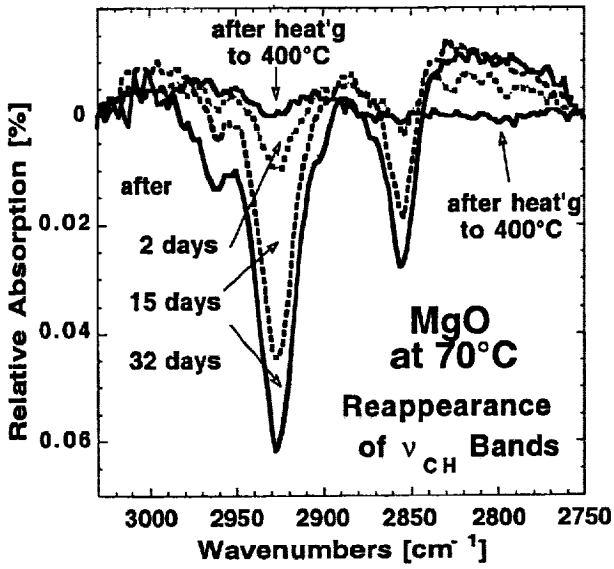

Figure 3: After heating for 14 hrs to 400°C the ν_{CH} bands in MgO vanish nearly completely but reappear during annealing at 70°C over a period of 32 days.

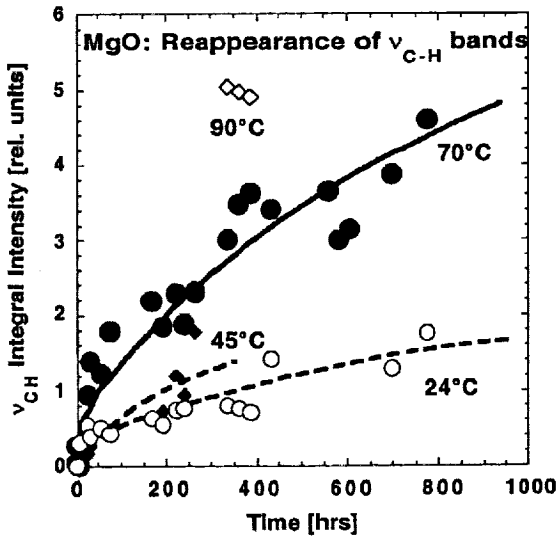

Figure 4: Integrated intensity of the ν_{CH} bands in the MgO crystal annealed at 70°C and other temperatures, plotted as a function of time. The symbols represent measured data, the lines parabolic fits.

Figure 4 plots the intensity of the ν_{CH} bands in MgO as a function of annealing time at 70°C (solid circles), at 24°C and 45°C (open circles and solid diamonds), and 90°C after the temperature controller malfunctioned, raising the temperature of the 45°C run to 90°C (open diamonds). The solid and broken

lines represent parabolic fits to the data. Obviously, the pyrolysis of the C–H bonds had caused H to disperse in the MgO matrix adjacent to the sites of the C_x entities. We do not know, however, whether hydrogen remains as H after pyrolysis or forms H_2. Upon annealing, H or H_2 diffuse back to the C_x chains, forming C-H bonds. If this process is controlled by 1-dimensional diffusion, the ν_{CH} intensity should increase linearly with the square root of time. Indeed, the parabolic fit to the 70°C data describes rather well the overall increase in the integral intensity of the ν_{CH} bands. During the first 32 days at 70°C the ν_{CH} bands regain about 10% of their original intensity. Assuming the same diffusion rate, 50% of the original intensity would be reached after 4500 days or 12.5 yrs.

The ν_{CH} bands of olivine disappear or nearly disappear upon heating to 300°C for 45 min. They reappear upon annealing, shifted by about 7cm^{-1} to lower wavenumbers, with a similar time constant as in MgO or slightly faster. After 32 days at 70°C the ν_{CH} bands of olivine had regained about 15% of their original intensity.

Discussion

The IR observations presented here can be summarized as follows:

(i) the ν_{CH} bands in the 2800–3050 cm^{-1} window arise from C-H entities in the crystal matrix;

(ii) nearly identical ν_{CH} bands are seen in the IR spectrum of laboratory-grown MgO and natural olivine crystals from the H_2O/CO_2–laden high pressure environment of the upper mantle;

(iii) the complexity of the ν_{CH} bands suggests polyatomic C_x entities with $-CH_2-$ and $-CH_3$ units;

(iv) the ν_{CH} bands disappear upon heating due to the pyrolysis of the C-H bonds; and

(v) the ν_{CH} bands reappear relatively rapidly, within a few days and weeks, upon annealing at moderate temperatures between room temperature and 70°C.

The presence of the ν_{CH} bands, their disappearance upon heating and reappearance upon annealing jointly point at a sequence of physical and chemical processes that occur in solid matrix. The ν_{CH} bands are consistent with C_x entities containing $-CH_2-$ and $-CH_3$. These C_x entities may represent "protomolecules" of those carboxylic, dicarboxylic and fatty acids that have been extracted from MgO and olivine crystals (1, 4). To understand how such protomolecules form, we review earlier work on the dissolution mechanism of H_2O and CO_2 that has laid the foundation for the study presented here.

Redox Conversion of Solute H_2O and CO_2

Classically, MgO crystallizing in the presence of H_2O and CO_2 can be treated as a three-component system with $Mg(OH)_2$, $MgCO_3$, and Mg-hydroxy-carbonates as distinct compounds (29). This suggests that, even if consideration is given to the possibility that H_2O and CO_2 may enter into solid solution, the only oxyanions will be OH^- and CO_3^{2-} as in eqs. [1] and [2]. However, the presence of H_2 molecules and of C-H entities suggests that the uptake of H_2O and CO_2 into solid solution leads to reactions that change the oxidation state of some of the solutes, producing H_2 and reduced C.

An early observation (30), made during the study of the degassing of finely divided MgO heavily doped with OH^-, provided the first hint towards a truly unusual reaction. In accordance to eq. [1], MgO containing OH^- should release nothing but H_2O. However, the finely divided MgO was found to release substantial amounts of molecular H_2, about 5,000 $H_2/10^6$ O (ppm). Such a large number of H_2

could not be accounted for by the very small number of transition metal impurities Me^{n+}, <5 ppm, that could have oxidized to $Me^{(n+1)+}$ by reducing H_2O according to: $2\ Me^{n+} + H_2O = 2\ Me^{(n+1)+} + O^{2-} + H_2$.

A further hint of what was happening came from the observation that the MgO began to emit O atoms above 600°C (30). This suggested peroxy anions, O_2^{2-}, decomposing according to the reaction $O_2^{2-} = 1/2\ O_2 + O^{2-}$ with O atoms being the primary product of disproportionation (29). This led to the proposition that the formation of H_2 molecules in the MgO matrix was coupled to the formation of peroxy anions by way of a hitherto unknown redox conversion involving OH^- pairs:

$$OH^- + OH^- = O_2^{2-} + H_2 \qquad [3]$$

The validity of this reaction was independently confirmed by a group at Oxford University (31) measuring the oxidizing properties of MgO prepared in a similar manner.

Eq. [3] is remarkable in as much as it implies a redox conversion in which the oxygens of OH^- acts as electron donors transferring electron density to the protons, thereby reducing them to H_2. Since a peroxy anion represents an excess O atom, this effectively describes a "water splitting" reaction, $H_2O = H_2 + O$. Though well documented (30, 31), this redox conversion has so far not been considered in the geosciences as an entry to better understand the interactions between H_2O and minerals.

Details of this reaction were further elaborated through an IR study of MgO crystals (17) which provided evidence that the conversion takes place among pairs of OH^- at specific defect sites, where Mg^{2+} vacancies are chargewise compensated by two OH^-. Around 500°C the OH^- pairs convert to O_2^{2-} plus H_2. Because of this, the ν_{OH} band at 3560 cm^{-1} in **Figure 1**, assigned to OH^- pairs at Mg^{2+} vacancy sites (17), is relatively weak. Since a majority of the OH^- pairs in the MgO matrix is affected, this leads to such a large number of H_2 molecules that the ν_{HH} band at 4150 cm^{-1} becomes observable as demonstrated by **Figure 1**.

In the same IR study (17) evidence was obtained that solute CO_2 in the MgO matrix exists in a chemically reduced form, probably as formate anions, CO_2^{2-}, with C occupying Mg^{2+} vacancy sites, and in an even more reduced form as CO^- anions with C on interstitial sites. This led to the proposition that dissolution of CO_2 in solid matrix is accompanied by a redox conversion similar to [3] in as much as O^{2-} acts as electron donor to reduce the C-bearing solutes:

$$CO_2 + 2\ O^{2-} = CO_2^{2-} + O_2^{2-} \qquad [4]$$

$$CO_2^{2-} = CO^- + O^- \qquad [5]$$

These reactions are not limited to MgO but apparently also occur in olivine $(Mg,Fe)_2SiO_4$ (23), even though, containing about 10% Fe^{2+}, upper mantle olivine may appear to be unlikely to contain oxygen oxidized to the peroxy stage (32). The ν_{CH} bands in olivine and their similarity to the ν_{CH} bands in MgO suggests that redox conversions whereby O^{2-} acts as electron donor may be common when H_2O and CO_2 dissolve in mineral matrices.

Segregation

Dissolution of H_2O and CO_2 in mineral matrices takes place during crystallization when the gas/fluid components partition between the melt and the growing crystals. The amount of H_2O and CO_2 taken up into solid solution depends upon the temperature (T) and partial pressures of the gas/fluid components (12). However, the equilibrium concentrations of the solute H_2O and CO_2

species decreases with decreasing T. This sets up a thermodynamic driving force to segregate the solutes to the surface or to any other sink that might be available inside the bulk (33, 34). The denser the crystal structure, the larger is the driving force. As long as the diffusion of the major cationic and anionic lattice constituents remains activated, i.e. at high T, segregation will simply lead to degassing of H_2O and CO_2. At lower T, as diffusion of cations and anions freezes, only those solutes can respond to the thermodynamic driving force that remain diffusively mobile. If some solutes that derive from H_2O and CO_2 retain diffusive mobility, they will segregate to the surface as well as to dislocations and other defects.

H_2 molecules are diffusively highly mobile in fused silica and quartz, which have relatively open structures (35). Though no diffusion coefficients for H_2 in MgO and olivine have been reported, given their small size and high polarizability, H_2 molecules are expected to retain diffusive mobility even in such dense structures down to relatively low temperatures. The case of C diffusion requires additional comments. By studying the temperature-time dependent behavior of solute C in MgO and olivine by x-ray photoelectron spectroscopy, $^{12}C(d,p)^{13}C$ depth profiling (22, 23), and secondary ion mass spectrometry (21) evidence was obtained that the diffusion of C involves the CO^- complex postulated in eq. [4], i.e. a C atom bonding to one O^- (21). When C occupies an interstitial site and bonds to O^-, the short C–O^- bond (~1.2 Å) will create a local volume contraction that lowers the activation energy barrier for the C atom to execute a diffusional jump to the next interstitial site. By bonding to a succession of O^- and executing a succession of interstitial jumps, solute C would thus be able to diffuse even through a densely packed O^{2-} matrix. Such a mechanism involves only transport of C atoms, because an O^- represents nothing but an electronic charge, i.e. a defect electron, moving from O^{2-} to O^{2-} in an otherwise stationary O^{2-} matrix.

Experimentally, during heating of MgO and olivine crystals, surface segregation of C sets in around 200°C (21-23), implying that, during cooling under geological conditions, solute C can be expected to segregate down to relatively low temperatures. The most widely available segregation sites inside crystals, however, are dislocations.

Dislocations can be classified into screw and edge dislocations (36). **Figure 5** depicts **(a)** an $a_o/2[100]$ screw dislocation and **(b)** the projection of two edge dislocations marking a subgrain boundary in MgO. The arrows in **(b)** point at the rows of Mg^{2+} cations along the edge dislocations that are under high compressive stress and therefore energetically unfavorable. To reduce the stress two possibilities exist: either remove this one highly stressed row of Mg^{2+} or remove in addition a row of O^{2-} next to it. In first case, the core of the dislocation becomes negatively charged. In the second case charge neutrality is maintained but at the expense of creating a larger void.

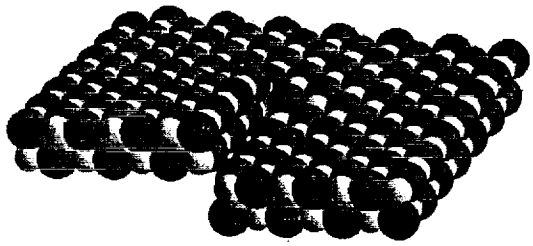

Figure 5a: An $a_o/2[100]$ screw dislocation in MgO showing how the (100) plane is displaced by $a_o/2$ after one turn. The large dark spheres indicate O^{2-} anions, the smaller light spheres Mg^{2+} cations.

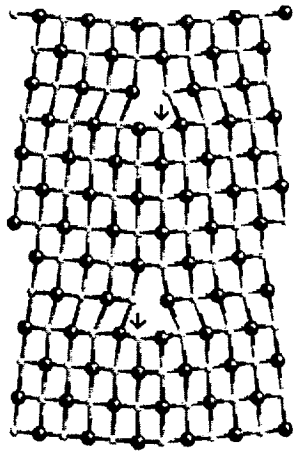

Figure 5b: Projection of two idealized edge dislocations generated as part of a subgrain boundary in MgO by the insertion of two half-planes of Mg^{2+} and O^{2-}. The arrows point at rows of Mg^{2+} cations that are under high compressive stress and therefore energetically unfavorable (after Harding et al., Phys. Rev. B 60, 2740-2746, 1999).

To model dislocations in compound crystals and avoid complications from net charges it is common practice to remove an equal number of cations and anion from the dislocation core (37, 38). We have chosen to remove only Mg^{2+} cations. This justified by the fact that dislocations in compound crystals are generally charged because , as they form and sweep through the structure, they collect cation vacancies (33, 34). Therefore, as their local stoichiometry deviates from the overall stoichiometry of the crystal, they become negatively charged. The $CO^{\cdot}$ complex postulated in eq. [4] is positively charged. Carrying a negative charge, dislocations will attract $CO^{\cdot}$ through long-range Coulomb interaction, facilitating the formation of polyatomic C_x entities through segregation (21).

Modeling Dislocations

As part of the work described here we modeled screw and edge dislocations in MgO and their interaction with $CO^{\cdot}$ by decomposing the process into three steps: first, we remove one row of Mg^{2+} cations; second, we convert the two adjacent rows of O^{2-} to $O^{\cdot}$, thus providing full charge compensation for the Mg^{2+} vacancies; and third, we allow C to segregate into the dislocation cores and to bond to $O^{\cdot}$.

When we add C atoms one by one to the dislocation cores, allowing them to also bond to each other, we build short C_x chains with the terminal C atoms bonded to two $O^{\cdot}$ of the MgO matrix. Taking into account the lattice parameter of MgO, $a_o = 4.21$ Å, the C–C bond length and bond angles, we can build aliphatic C_x chains with $n \leq 4$ that are strainfree, even without taking into account a possible relaxation of the MgO matrix around the dislocation cores (37, 38). In the case of the $a_o/2[100]$ screw dislocation, we find the best fit for C_4 units in trans-configuration. In the case of subgrain boundary dislocations, in order to fit into the dislocation core, the C_4 units have to buckle into a cis-configuration. For $n > 4$ the C–$O^{\cdot}$ bonds at the terminal C positions become progressively more strained and go out of phase with respect to the surrounding MgO matrix.

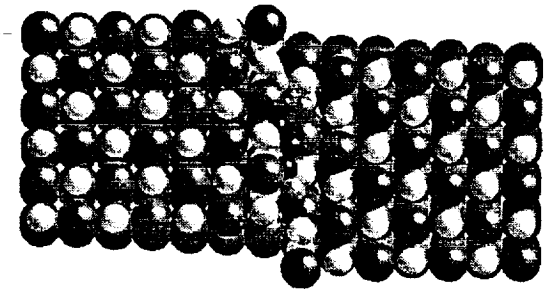

Figure 6a: Stack of MgO (100) planes with a vertical $a_o/2[100]$ screw dislocation in the center, viewed at right angle. The screw dislocation is decorated by one $[O_2C\text{-}C\text{-}C\text{-}CO_2]$ unit in the energetically favorable trans-configuration with the medium size light grey spheres representing O^-.

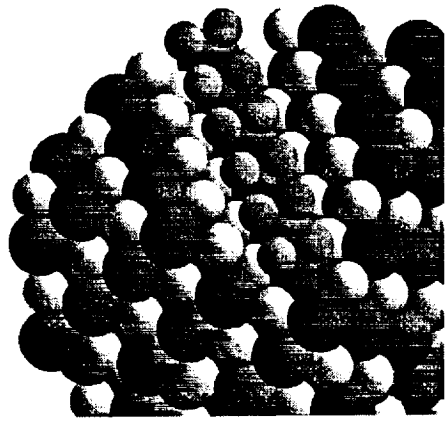

Figure 6b: Oblique view of an edge dislocation in MgO with one row Mg^{2+} removed and two rows of O^{2-} changed to O^- (lighter gray spheres).

Figure 6a shows a cut through a stack of MgO planes containing an $a_o/2[100]$ screw dislocation. Its core is decorated with a C_4 unit in trans-configuration and its terminal C atoms bonding to two O^- each, resulting an $[O_2C\text{-}C\text{-}C\text{-}CO_2]$ unit. **Figure 6b** provides an oblique view of an edge dislocation with one row of Mg^{2+} cations removed and two rows of O^- lining the core. In **Figure 6c** C atoms are segregated into the axis of the dislocation core forming $[O_2C\text{-}C\text{-}C\text{-}CO_2]$ units in cis-configuration.

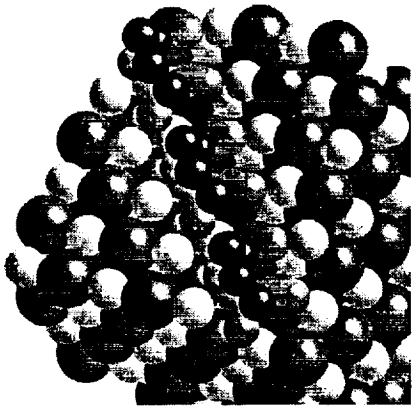

Figure 6c:
Same edge dislocation with C_4 units segregated into its core. Because of mismatch with the surrounding MgO matrix the $[O_2C\text{-}C\text{-}C\text{-}CO_2]$ units would have to adopt the energetically less favorable cis-configuration.

Stereochemical Control

Dislocations provide for a stereochemically constrained environment that forces the segregating C atoms into C_x chains. Depending on the specific conditions and/or the mineral structure different chain length C_x entities might form. In other types of lattice defects solute C atoms may segregate to form cyclic or branched C_x entities. We are here confronted with the possibility that the mineral matrices in which C_x entities precipitate influence or even control the shape and size of these C_x segregates. Hence, when these minerals weather, they will release a set of stereochemically preselected organic

molecules. Such a mechanism is expected to produce a smaller number of different compounds than reactions in the gas phase, liquid phase or by surface catalysis.

On the basis of the simulations presented here it appears that linear C_x entities with n = 4 in trans-configuration might be energetically favored in screw dislocations in MgO. With their terminal C atoms bonding stress free to two O^- each, they would anchor the $[O_2C\text{-}C\text{-}C\text{-}CO_2]$ entity to the MgO structure. Adding H_2 leads to $-CH_2-$ and to entities that may be described as $[O_2C(CH_2)_2CO_2]$ or, more generally, as C_x–H_y–O_z entities. The $-CH_2-$ therein would give rise to two ν_{CH} bands arising from the symmetrical and asymmetrical C-H stretching mode similar to these modes in the IR spectrum of polyethylene (25). The two strongest ν_{CH} bands at 2926 and 2855 cm^{-1} in the IR spectrum of MgO (see **Figure 2**) would then have to be assigned to $-CH_2-$ sections of linear aliphatic chains of the general formula C_x–H_y–O_z, formed through segregation of C and H_2 into dislocations.

Solvent extraction experiments of crushed MgO single crystals produced a suite of carboxylic and dicarboxylic acids from C_2 to C_4 with succinic acid, $HOOC(CH_2)_2COOH$, being a major component (4), pointing at dislocation-bound $[O_2C(CH_2)_2CO_2]$ entities as possible protomolecules. Extraction experiments with crushed olivine crystals yielded longer chain-length fatty acids, C_6 to C_{12} (1), suggesting that longer-chain C_x–H_y–O_z entities had formed in the olivine matrix. The difference in chain length may reflect differences between the structures of MgO and olivine. Alternatively, because the olivine crystals had cooled at a much slower rate in a volcanic pipe (24), there was more time for the segregation of solute C into the dislocations, thus producing longer-chain C_x–H_y–O_z entities. These longer C_x–H_y–O_z entities may be the reason why, as seen in **Figure 2**, the ν_{CH} bands from the olivine crystal are narrower than the ν_{CH} bands from the MgO crystal, even though MgO has a simpler structure and would thus be expected to provide a more uniform local lattice environment.

Prebiotic Evolution

Many pathways are known by which organic matter can be synthesized through gas phase, liquid phase, and gas-solid and liquid-solid reactions. How much could have been produced under early Earth conditions depends on whether or not the atmosphere at that time was reducing. Table I gives estimated production rates (8) for two cases: (i) a highly reducing atmosphere rich in methane, hydrogen and ammonia, and (ii) an intermediate atmosphere, still reducing, with an H_2/CO_2 ratio of 1:10. More likely, however, (39) the early atmosphere was non-reducing. In this case almost no organics would have been produced in the atmosphere by the processes indicated.

Source	Highly Reducing Atmosphere [g yr^{-1}]	Intermediate Atmosphere [g yr^{-1}]
UV photolysis	1×10^{15}	3×10^{11}
Electric Discharges	3×10^{12}	3×10^{10}
Shocks from Large Impacts	2×10^{13}	4×10^{5}
Shocks from Meteors	4×10^{12}	8×10^{4}
Totals	$\sim 1 \times 10^{15}$	$\sim 5 \times 10^{11}$

Table I: Major source of prebiotic organics for two candidate early atmospheres (after 8).

Interplanetary Dust Particles (IDPs) in the size range 0.6 - 60 μm and containing up to 10% carbon provide an exogenous source for organics. Since they are slowly decelerated upon entry in the Earth's atmosphere, their organics survives the entry. Today the Earth captures between 3×10^9 and 1×10^{10} g yr^{-1} IDPs, contributing between 3×10^8 and 1×10^9 g yr^{-1} organics (40, 41). The rate of IDPs capture after the period of heavy bombardment was probably much higher (8), maybe 2-3 orders of magnitude higher, thus delivering about 10^{11} - 10^{12} g yr^{-1} of organics.

The work presented here points at a source of organics that is different from all other sources discussed so far in the literature. If C_x–H_y–O_z protomolecules form in mineral matrices, they will turn into organic molecules during weathering (1, 4). The organic molecules thus liberated may be difficult to synthesize by any of the other reaction pathways given in Table I. Note that these reaction pathways invariably involve large departures from thermodynamic equilibrium, mostly in form of very high temperatures for a very short period of time. By contrast, the assembly of C_x–H_y–O_z protomolecules inside the minerals and their release during weathering are processes that occur under much more benign conditions, at moderate or even ambient temperatures, and not too far from equilibrium.

We can estimate how much organics could have been supplied to the Earth through the weathering cycle. On the early continents many of the rocks exposed at the surface were probably peridotites, rich in olivine and other minerals that weather rapidly under the effect of CO_2-saturated meteoric water. Assume that the volume of rock recycled was of the order of 3 km^3/yr (10^{16} g/yr), the same as today (42), and that their solute C content was of the order of 100 ppm as in olivine (27, 28). If 1/10 of this solute C or 10 ppm were in form of C_x–H_y–O_z protomolecules, the weathering cycle would have produced organics at a rate of about 10^{11} g/yr. The production would have been unaffected by the atmospheric composition and independent of any delivery of meteors and comets to the early Earth (43). Furthermore, the production rate would have been sustained over long time or even increased with the growth of the continents. If we include subsurface weathering such as serpentinization of peridotites and leaching of rocks by hydrothermal fluids, the production rate of organics would be even higher.

Conclusions

The assembly protomolecules by way of solid state processes shows that "organic" chemistry can take place in the dense, hard matrix of igneous minerals. This opens new aspects to the study of stereochemically constrained complex organic molecules, synthesized under prebiotic conditions. Such processes may have provided large amounts of biochemically relevant organics to the early Earth.

Acknowledgments

This work was supported by NASA's Exobiology Program under RTop 344-38-22-15. A. S. participated through the grant # PHY-9605147 from the National Science Foundation as part of the REU (Research Experience for Undergraduates) Program at the Department of Physics, San Jose State University. J. S. thanks the NASA Astrobiology Academy for the opportunity to spend the Summer 2000 at the NASA Ames Research Center. We thank Bishun Khare for the opportunity to use the Nicolet Nexus 670 FT-IR spectrometer.

References

1. Freund, F., Gupta, A. & Kumar, D. (1999) *Origins Life Evol. Biosphere* **29,** 489-509.
2. Freund, F. & Ho, R. (1996) in *Circumstellar Habitable Zones*, ed. Doyle, L. R. (Travis House Publ., Menlo Park, CA), pp. 71-98.
3. Butler, C. T., Sturm, B. J. & Quincy, R. B. (1971) *J. Cryst. Growth* **8,** 197-204.
4. Gupta, A. & Freund, F. (1998) in *Lunar & Planetary Science Conference* (Lunar & Planetary Institute, Houston, TX), Vol. 29.
5. McCollom, T. M., Ritter, G. & Simoneit, B. R. T. (1999) *Origins of Life Evol Biosphere* **29,** 153-166.
6. Bernd, M. E., Allen, D. E. & Seyfied, W. E. (1996) *Geology* **24,** 351-354.
7. Hennet, J. C., Holm, N. G. & Engel, M. H. (1992) *Naturwiss* **79.**
8. Chyba, C. F. & Sagan, C. (1992) *Nature* **355,** 125-132.

9. Chang, S. (1993) in *The Chemistry of Life's Origins*, ed. Greenberg, J. M. (Kluwer Acad. Publ., Amsterdam), pp. 259-299.
10. Rossman, G. R. (1996) *Phys. Chem. Minerals* **23,** 299-304.
11. Bell, D. R. & Rossman, G. R. (1992) *Science* **255,** 1391-1397.
12. Burnham, W. C. (1979) in *The Evolution of Igneous Rocks, Fifthieth Anniversary Perspectives*, ed. Yoder, H. S. (Princeton Univ. Press, Princeton, NJ), pp. 439-482.
13. Spera, F. J. & Bergman, S. C. (1980) *Contrib. Mineral. Petrol.* **74,** 55-66.
14. Fine, G. & Stolper, E. (1985) *Contrib. Mineral. Petrol.* **91,** 105-121.
15. Mathez, E. A. (1987) *Geochim. Cosmochim. Acta* **51,** 2339-2347.
16. Tingle, T. N., Mathez, E. A. & Hochella, M. F. (1991) *Geochim. Cosmochim. Acta* **55,** 1345-1352.
17. Freund, F. & Wengeler, H. (1982) *J. Phys. Chem. Solids* **43,** 129-145.
18. De Remigi, J. & Welsh, H. L. (1970) *Can. J. Phys.* **48,** 1622-1627.
19. Tsong, I. S. T., Knipping, U., Loxton, C. M., Magee, C. W. & Arnold, G. W. (1985) *Phys. Chem. Minerals* **12,** 261-270.
20. Mathez, E. A., Blacic, J. D., Berry, J., Maggiore, C. & Hollander, M. (1987) *J. Geophys. Res.* **92,** 3500-3506.
21. Freund, F. (1986) *Phys. Chem. Minerals* **13,** 262-276.
22. Kathrein, H., Gonska, H. & Freund, F. (1982) *Appl. Phys.* **30,** 33-41.
23. Oberheuser, G., Kathrein, H., Demortier, G., Gonska, H. & Freund, F. (1983) *Geochim. Cosmochim. Acta* **47,** 1117-1129.
24. Frey, F. A. & Prinz, M. (1978) *Earth Planet. Sci. Lett.* **38,** 129-176.
25. Spectra, S. S. (1980) *Infrared Spectra Atlas of Monomers and Polymers* (Chemical Concepts/Wiley.
26. Freund, F. (1986) *Phys. Chem. Minerals* **13,** 280.
27. Minaev, V. M., Shilobreeva, S. N. & Kadik, A. A. (1995) *J. Radioanal. Nucl. Chem.* **189,** 147-155.
28. Kadik, A. A., Shilobreeva, S. S., Minaev, V. M. & Kovalenko, V. I. (1996) in *Lunar and Planetary Science XXVII* (Lunar and Planetary Institute, Houston, TX), Vol. 27, pp. 631-632.
29. Wells, A. F. (1984) *Structural Inorganic Chemistry* (Oxford Clarendon Press, Oxford).
30. Martens, R., Gentsch, H. & Freund, F. (1976) *J. Catalysis* **44,** 366-372.
31. Praliaud, H., Coluccia, S., Deane, A. M. & Tench, A. J. (1979) *Chem. Phys. Lett.* **66,** 44-47.
32. Freund, F. & Oberheuser, G. (1986) *J. Geophys. Res.* **91,** 745-761.
33. Nowotny, J. (1989) in *Surfaces and Interfaces of Ceramic Materials.*, eds. Dufour, L. C., Monty, C. & Petot-Ervas, G. (Kluwer Academic Publ., Amsterdam), pp. 205-239.
34. Pennycock, S. J., Chisholm, M. F., Yan, Y., Duscher, G. & Pantelides, S. T. (1999) *Physica B* **274,** 453-457.
35. Shelby, J.E (1977) J. Appl. Phys. 48, 3387-3394.
36. Philibert, J. (1983) in *Basic Properties of Binary Oxides*, eds. Dominiguez-Rodrigues, A., Castaing, J. & Marques, R. (Univ. Sevilla, Sevilla, Spain), pp. 279-296.
37. Harris, D. J., Khan, M. A. & Parker, S. C. (1999) *Phys. Chem. Minerals* **27,** 133-137.
38. Harding, J. H., Harris, D. J. & Parker, S. C. (1999) *Phys. Rev. B* **60,** 2740-2746.
39. Kasting, J.F. (1993) Science 259, 920-926.
40. Anders, E.(1989) Nature 342, 255-257.
41. Love, S.G. & Brownlee, DE (1993) Science 262, 550-553.
42. Koster von Groos, A.F. (1988) J. Geophys. Res., 93, 8952-8958.
43. Chyba, C. F., Thomas, P. J., Brookshaw, L. & Sagan, C. (1990) *Science* **249,** 366-373.

Special Issue of the Journal of Geodynamics to be published 2002

Charge generation and propagation in igneous rocks

Friedemann Freund

Department of Physics, San Jose State University, San Jose, California 95192-0106
and SETI Institute/NASA Ames Research Center, MS 239-15 Moffett Field, California 94035-1000, USA
Tel: +1-650-604-5183; Fax: +1-650-604-1092; e-mail: ffreund@mail.arc.nasa.gov

Abstract

Various electrical phenomena have been reported prior to or concurrent with earthquakes such as resistivity changes, ground potentials, electromagnetic (EM), and luminous signals. Doubts have been raised as to whether some of these phenomena are real and indeed precursory. One of the reasons for uncertainty is that, despite of decades of intense work, there is still no physically coherent model. Using low- to medium-velocity impacts to measure electrical signals with microsecond time resolution, it has now been observed that when dry gabbro and diorite cores are impacted at relatively low velocities, ~100 m/s, highly mobile charge carriers are generated in a small volume near the impact point. They spread through the rocks, causing electric potentials exceeding +400 mV, EM, and light emission. As the charge cloud spreads, the rock becomes momentarily conductive. When a dry granite block is impacted at higher velocity, ~1.5 km/s, the propagation of the P and S waves is registered through the transient piezoelectric response of quartz. After the sound waves have passed, the surface of the granite block becomes positively charged, suggesting the same charge carriers as observed during the low-velocity impact experiments, expanding from within the bulk. During the next 2-3 ms the surface potential oscillates, indicating pulses of electrons injected from ground and contact electrodes. The observations are consistent with positive holes, e.g., defect electrons in the O^{2-} sublattice, traveling via the O 2p-dominated valence band of the silicate minerals. Before activation, the positive holes lay dormant in the form of electrically inactive positive hole pairs, PHP, chemically equivalent to peroxy links, $O_3X/^{OO}\backslash XO_3$, with $X=Si^{4+}$, Al^{3+}, etc. PHPs are introduced into the minerals by way of hydroxyl, O_3X-OH, which all nominally anhydrous minerals incorporate when crystallizing in H_2O-laden environments. The fact that positive holes can be activated by low-energy impacts, and their attendant sound waves, suggests that they can also be activated by microfracturing. Depending on where in the stressed rock volume the charge carriers are activated, they will form rapidly moving or fluctuating charge clouds that may account for earthquake-related electrical signals and EM emission. Wherever such charge clouds intersect the surface, high fields are expected, causing electric discharges and earthquake lights.

1. Introduction

To more fully understand the earthquake process and allow for the inclusion of electric signals it is necessary to re-evaluate the standard earthquake model as it has evolved historically (Bolt, 1988; Eiby, 1980; Meyer, 1977; Rikitake, 1976). According to the standard model, as rocks in earthquake-prone regions in the Earth's crust are subjected to tectonic stress, they pass through several stages that manifest themselves in ways that lead to measurable effects at the surface of the Earth.

In simple terms these effects can be described as follows: When a rock volume under lithostatic load is compressed, the rocks begin to buckle and undergo microfracturing, causing uplift and tilt at the Earth's surface. The microfracturing releases radon and other gases. Within the crust the electrical conductivity decreases because of the closure of existing pores, then increases as new microcracks are created or saline pore fluids are forced out to form interconnected intergranular water films. As the

stresses continue to build, larger fissures are thought to allow the intergranular brines to coalesce and further increase the electrical conductivity.

Interestingly, within the framework of this standard model, the rocks themselves play only a passive role. Any change in their electrical conductivity is attributed to the saline pore fluids with which they are saturated and which redistribute in response to the externally applied stress – from closed pores to intergranular brine films to brine-filled fissures. Such a redistribution of fluids, if it occurs, would explain the reported changes in overall electrical conductivity, derived from field measurements. However, a redistribution of fluids can hardly explain the emission of electrical and electromagnetic signals from a given rock volume, except by assuming that, as the brines are forced to flow through narrow fissures and pores, they give rise to streaming potentials (Bernabé, 1998; Draganov et al., 1991; Morrison et al., 1989).

The standard model accords importance to water as the prime cause of electrical conductivity of rocks because crustal earthquakes occur along faults zones. Each fault contains highly deformed, fractured, mellinitized rocks that allow penetration of surface water to 10 km or more (Park, 1997a,b). Since the conductivity of even moderately saline water far exceeds the conductivity of solid rocks, the average conductivity of a rock volume that includes a fault zone is likely to be dominated by the conductivity of the narrow zones of brine-impregnated faults.

At the same time, faults are bounded on either side by large volumes of rocks that often may not contain much water either in closed pores, as intergranular films or in open fissures. The question arises how the rock volume outside the narrow fault zones contributes to the overall electrical conductivity and specifically to the generation of electrical signals.

This paper presents evidence that dry rocks, in particular dry igneous rocks, can become a source of highly mobile electronic charge carriers. These charge carriers not only cause an increase in the electrical conductivity, but they also appear to be capable of propagating through the rocks as a charge cloud.

1.1. Precursor Signals

There seems to be a growing consensus that at least some electrical earthquake precursor signals are plausible (Bernard, 1992; Johnston, 1997), though the standard model does not provide a physically coherent concept. This is particularly relevant to those electrical signals that require charges to propagate through the rock volume (Dobrovolsky et al., 1989; Park, 1997a). Such signals are controversial (Geller, 1997; Michael, 1996; Pham et al., 1998). In some cases such as at Parkfield, California, along and across the San Andreas fault system no clear changes in the conductivity or any other electric effects related to seismicity have been identified (Park, 1997b).

Broadly speaking, electric and EM signals can be divided into three categories: (1) ground potentials, (2) EM emission and luminous phenomena, and (3) perturbations in the ionosphere.

1. Ground potentials can be generated as "streaming potentials" when saline water, moving through porous rocks, entrains ionic charges (Bernabé, 1998; Draganov et al., 1991; Morrison et al., 1989). Another way is through stress applied to rocks containing piezoelectric minerals such as quartz (Bishop, 1981; Finkelstein et al., 1973; Morat and Le Mouel, 1987, 1992), maybe also in the absence of piezoelectric minerals (Varotsos et al., 1997). The transmission of substantial stress over large distances has been debated (Geller, 1996; Huang and Ikeya, 1998; Masood, 1995).

(2) Low-frequency EM emissions reported from field observations have received some level of recognition as stated in reviews by Johnston and Parrot (1989), Park et al. (1993), and Johnston (1997). Such signals have been documented in connection with the 1989 Loma Prieta earthquake in California (Fraser-Smith et al., 1990), though their origin remains uncertain (Bernard, 1992, Merzer and Klemperer, 1997). EM emissions were also recorded during the 1989 Ito seismic swarm in Japan (Fujinawa and Takahashi, 1990). Detection of EM signals is pursued by groups in Japan, China, and

countries of the former Soviet Union (Molchanov et al., 1992; Serebryakova et al., 1992) and in China (Zhijia, 1989). Puzzling and in part intertwined with folklore (Tributsch, 1983) are luminous phenomena reported to accompany some large earthquakes (Derr, 1973; Hedervari and Noszticzius, 1985), occasionally also weak events such as in 1988 in the Saint John region of Canada (Quellet, 1990). Earthquake lights were photographed during the 1966 earthquake at Matsushiro, Japan (Derr, 1986). Piezoelectricity from quartz-bearing rocks (Finkelstein et al., 1973) and sonoluminescence (Johnston, 1991) have been suggested though full laboratory confirmation seems to be still lacking.

(3) Ionospheric perturbations over earthquake regions have been observed during the 1964 Alaskan earthquake (Davis and Baker, 1965) and over parts of continental Asia (Bilichenko et al., 1990; Chmyrev et al., 1986; Drobgev et al., 1978; Galperin et al., 1985; Kustov and Liperovsky, 1988; Larkina et al., 1988), over Japan (Molchanov and Hayakawa, 1998a,b) such as over Kobe a few days before and after the January 1995 earthquake (Molchanov et al., 1998), and over Taiwan (Liu et al., 2000), including a few days before and after the September 1999 Chichi earthquake (Lee et al., 2000)

1.2 Known Sources of Electric Charges in Rocks

Known processes for the generation of electric charges are streaming potentials, piezoelectricity, triboelectricity/triboluminescence, spray and contact electrification.

Streaming potentials arise when weakly conducting liquids such as fuel or transformer oil are pumped through pipes and conduits (Oommen, 1988). In nature they occur when saline water moves through porous rocks, entraining solvated ions of one sign, while the charge-balancing counterions remain adsorbed to the rocks. The magnitude of the potentials is limited by the return currents flowing along the double layer (Bernabé, 1998; Draganov et al., 1991; Morrison et al., 1989).

Piezoelectricity describes the phenomenon that, when a stress is applied to certain crystals in certain crystallographic directions, opposite sides of the crystals become instantly charged (Finkelstein et al., 1973). Quartz is the only mineral in a piezoelectric symmetry class that is abundant in nature. In a stressed volume with quartz crystals in random orientation the piezopotentials tend to cancel.

Triboelectricity and triboluminescence describe phenomena that occur when crystals are abraded, indented or fractured. On an atomic level, rapidly moving dislocations create exciton pairs, i.e., electrons and holes, which luminesce upon recombination. Advancing fracture wedges cause charge separation on either the opposing sides (Enomoto and Hashimoto, 1990; Hadjicontis and Mavromatou, 1994; Yoshida et al., 1997, 1998; Brady and Rowell, 1986).

Spray electrification is a term used to describe the charging of water droplets by splashing or spraying (Loeb, 1958). Assuming that pore water evaporates suddenly when seismic waves disrupt surface rocks and cause intense local heating, spray electrification has been invoked by Lockner et al. (1983) as a possible mechanism to explain earthquake lights.

Contact electrification is a fundamental process that occurs whenever two dissimilar materials are brought in contact. It arises even in insulators because, however low their conductivity, they will always have a nonzero density of electronic charges. These charges define a Fermi level similar to the Fermi level in semiconductors. Upon contact, charges flow across the contact point until the Fermi levels are equalized. An exemplary experiment describing charge transfer between mica and quartz has been reported by Horn and Smith (1992).

However, none of the mechanisms or processes listed stands out as a candidate for bringing the electrical, electromagnetic and luminous phenomena together and present a coherent physical model. There seems to be only one way out: we have to consider the possibility that, despite decades of intense studies in laboratories worldwide, rocks may contain charge carriers that have not yet been properly identified.

1.3 Less Well-Known Source of Electric Charges in Rocks

Electronic charge carriers in rocks are generally thought to be of minor concern because most minerals are good insulators. Electronic charge carriers can be electrons or defect electrons, the latter known as "holes." Both, electrons and holes can be associated with transition metal cations that change their oxidation states. In some minerals where an electronic exchange between neighboring transition metal cations can take place, hole conductivity occurs. However, except in cases where Fe^{2+} and Fe^{3+} are direct neighbors on crystallographically well-defined sites such as in magnetite, hole conductivity is rare. This is supported by the fact that even Fe-rich pyroxene and olivine show negligible electronic conductivity via their cation sublattices (Schock and Duba, 1985; Shankland, 1981).

What is hardly ever recognized is the fact that oxygen can also exist in two oxidation states: as O^{2-} in the common 2- oxidation state and as O^- in the somewhat uncommon 1- oxidation state. Because textbooks invariably formulate mineral structures with the tacit assumption that oxygen is never anything but O^{2-}, it is widely assumed that oxygen is locked into its 2- oxidation state. However, given special local lattice conditions to be outlined below, O^{2-} can convert to O^-. An O^- in an O^{2-} matrix represents an electronic charge carrier, a hole, but it is different from the holes that reside on the cation sublattice. To underscore this difference an O^- in the O^{2-} sublattice is designated as a "positive hole".

The remainder of this paper will be dedicated to positive holes and their possible role in generating electric signals in rocks.

1.4. Nature of the Positive Holes

Before addressing the question how oxygen in the –1 oxidation state is introduced into minerals and rocks, I would like to summarize what we believe to know about positive holes and about their propagation through rocks.

From a chemist's perspective, an O^- is an oxygen anion with an incomplete valence shell, 7 electrons instead of the usual 8. An O^- is a radical, and writing it as $O^\bullet$ is equally valid. If the O^- is part of an XO_4^{4+} complex ($X = Si^{4+}$, Al^{3+}, etc.), it might be written either as XO_4^{3+} or as $O_3X/^{O^\bullet}$. Being radicals, O^- _ $O^\bullet$ and XO_4^{3+} _ $O_3X/^{O^\bullet}$ are unstable. They can react with each other by pairing up to form a positive hole pair, PHP, chemically equivalent to a peroxy anion, $O^- + O^- = O_2^{2-}$ or a peroxy link $O_3X/^{O^\bullet} + {}_\bullet O/XO_3 = O_3X/^{OO}\backslash XO_3$. Such peroxy links can be thermodynamically stable, if they are associated with certain defect sites in the host mineral structure (King and Freund, 1984). Noteworthy is also the fact that the O^-–O^- distance is very short, generally less than 1.5 Å, about half the O^{2-}...O^{2-} distances in most mineral structures, 2.8-3.0 Å. The shortness of the O^-–O^- bond implies a small partial molar volume of the peroxy-bound O^-, and thus a tendency to be favored by high pressure.

From a physicist's perspective, the $O^\bullet$ or $O_3X/^{O^\bullet}$ represents a positive hole as defined above, i.e. an electronic charge. A peroxy link then represents a self-trapped positive hole pair, PHP, immobile and electrically inactive (King and Freund, 1984). Most positive holes in minerals will be found in form of PHPs. Because the PHPs are electrically inactive and do not manifest themselves in any other easily recognizable way, the very presence of PHPs in minerals has been overlooked. However, PHPs may dissociate by breaking the O^-–O^- bond, thus releasing a positive hole charge carrier.

In the band model an insulator is defined as a material with a wide energy gap in which all valence band states are filled. No electrons can flow, and the conductivity is zero. Even in the presence of PHPs, the material remains an insulator. However, if a PHP dissociates, it introduces holes into the valence band, causing the insulator to become a p-type semiconductor.

The propagation of positive holes through an oxide or silicate matrix can be discussed in terms of electron hopping. If one O^{2-} in a sea of O^{2-} changes to O^-, it creates a situation whereby electrons from neighboring O^{2-} can hop onto the O^- site. In first approximation the hopping frequency is controlled by phonons, e.g. by collisions with neighboring O^{2-}, which typically occur at a frequency of the order of 10^{12} s^{-1}. By multiplying the phonon frequency with the hopping distance, ~3 Å, and considering a probability factor of 1/3 that the electron hops in a given direction, we can estimate the maximum speed at which a positive hole could propagate, 100-300 m/s. Because the positive holes travel via the O 2p-dominated valence band, they can cross grain boundaries without being scattered or annihilated.

1.5. How are Positive Holes Introduced into Minerals and Rocks?

In this section I discuss one way by which PHPs are introduced into mineral structures. As the basic reaction involves only the O^{2-} sublattice, the essential features can be described by looking at a simple oxide structure, MgO.

When MgO crystallizes in the presence of H_2O, it incorporates small amounts of H_2O in form of OH^-, preferentially as OH^- close to Mg^{2+} vacancy sites:

$$(H_2O)_{dissolved} + (O^{2-})_{structure} \_ (OH^-)_{structure} + (OH^-)_{structure}. \qquad (1)$$

It has been noted early (Martens et al., 1976) that such OH^- pairs can undergo a previously unknown redox conversion whereby they split off molecular H_2 and form two O^- which in turn undergo self-trapping to a peroxy anion, O_2^{2-}, e.g., a PHP:

$$(OH^-)_{structure} + (OH^-)_{structure} = (H_2)_{structure} + (O_2^{2-})_{structure}. \qquad (2)$$

The presence of H_2 molecules in MgO single crystals was confirmed by infrared spectroscopy (Freund and Wengeler, 1982). Evidence for PHPs was obtained by electrical conductivity (Freund et al., 1993), magnetic susceptibility, dielectric polarization measurements as well as by measuring other less direct physical properties (Freund et al., 1994). Though all these studies were done at ambient pressure, the fact that the partial molar volume of O^- in the peroxy bond is much smaller than that of O^{2-} and OH^-, suggests that pressure should favor the redox conversion of OH^- pairs to H_2 plus peroxy.

Silicate minerals, even those that are nominally anhydrous, also incorporate traces of H_2O whenever they crystallize in H_2O-laden magmatic or metamorphic environments (Rossman, 1996). Initially they form O_3X–OH pairs:

$$(H_2O)_{dissolved} + (O_3X/^{O}\backslash XO_3)_{structure} \_ (O_3X/^{OH}{}_{HO}/XO_3)_{structure} \quad (3)$$

However, as the OH^- pairs in MgO, O_3X-OH pairs in silicates undergo a redox reaction whereby they also reduce two H^+ to H_2 and oxidize two O^{2-} to O^-, which in turn combine to form a peroxy link, typically between two adjacent SiO_4 tetrahedra:

$$(O_3X/^{OH}{}_{HO}/XO_3)_{structure} = (H_2)_{structure} + (O_3X/^{OO}\backslash XO_3)_{structure}. \quad (4)$$

Peroxy links in SiO_2 have been studied theoretically by Edwards and Fowler (1982) and experimentally (Friebele et al., 1979; Freund and Masuda, 1991). The O^-–O^- bond can break easily, releasing a positive hole. Continuing from (2) and (4) we have

$$(O_2^{2-})_{structure} = (O^- + O^-)_{structure} \qquad (5)$$

$$(O_3X/^{OO}\backslash XO_3)_{structure} = (O_3X/^{O\bullet}\ \bullet O/XO_3)_{structure}. \qquad (6)$$

The dissociation of the peroxy bond according to (5) and (6) turns the insulator into a semiconductor. Since the positive holes are the only mobile charge carriers and no electrons are generated at the same time, the semiconductor is purely p-type.

In MgO, where PHPs are associated with Mg^{2+} vacancies (Freund et al., 1993, 1994), the two positive holes compensate for the charge of the missing Mg^{2+} cation. When the PHP dissociates and one positive hole becomes a mobile charge carrier, the other positive hole stays behind at the Mg^{2+} vacancy site but is immobile because Mg^{2+} vacancies only diffuse at temperatures above 700°C. Similar analogous arguments can be made for PHP in SiO_2 or feldspars, where the XO_4^{4-} are linked at all four corners by $O_3X–O–XO_3$ bonds. After $O_3X/^{OO}\backslash XO_3$ dissociation according to equation (6) one XO_4^{4+} and one XO_4^{3+} remain. This configuration represents a negative charge that is stationary compared to the positive hole which is mobile.

For understanding the experiments to be described below it is important to note that, when positive holes are the only mobile charge carriers, their mutual electrostatic repulsion forces them to the surface. This outward flow of positive charges continues until balanced by the electric field that builds up between the surface and the negatively charged bulk (King and Freund, 1984). For the impact experiments this has two consequences: (1) The magnitude of the positive surface potential becomes a function of the dielectric contrast between the bulk and air, __~ 1. Assuming that the rock has a dielectric constant __~ 10 the calculated flat surface potential in vacuum, __= 1, is +420 mV. (2) The electric field at the surface becomes a function of the concentration of positive holes in the bulk. When their concentration increases from 10 ppm to 100 ppm (10^{17} to 10^{18} cm^{-3}), the surface field increases from 1.2×10^5 to 4×10^5 V/cm, high enough to consider dielectric breakdown of the surrounding air.

1.6. Why Impact Experiments?

The impact experiment described here were not undertaken in order to simulate as closely as possible a specific natural condition, but to achieve two basic goals. First, to demonstrate that positive hole-type charge carriers can be generated from pre-existing, dormant PHP precursors. Second, to gain insight into the somewhat surprising properties of these charge carriers as they propagate through the rocks. The idea came from prior single crystal fracture experiments, using MgO as a well-characterized oxide material (Dickinson et al., 1986) and olivine. These experiments suggested that the acoustic waves or dislocation movements generated by the brittle fracture were enough to cause PHP dissociation according to equations (5) and (6).

If the weak acoustic waves generated by brittle fracture are capable of activating the positive holes, the question arose whether microfracturing in rocks prior to an earthquake might also activate positive holes, at least in a small volume around the microfracture event. Likewise, if the stresses cause plastic deformation (creep) of the rocks and, hence, dislocation movements, positive holes are likely to be activated. Assuming that microfracturing and creep become pervasive as the tectonic stresses reach critical levels, activation of positive holes and their outflow from the stressed volume could represent the long-sought charge generation mechanism responsible for preseismic electric and electromagnetic signals that have been reported from the field prior to earthquake activity.

2. Experimental Procedures

2.1 Low-Velocity Impact Experiments

Low-velocity impact experiments were conducted as described earlier (Freund and Borucki, 1999), using stainless steel, 1/8-inch to 1/4-inch (3.1-6.3 mm) diameter projectiles at close to 100 m/s delivering 0.06 - 0.43 J kinetic energy to cylindrical rock cores, 3/4-inch (20 mm) diameter and up to 4-

inch (100 mm) long. The shots left small whitish marks on the front face of the rock cores and led to chipping and fracture.

The sensors included: (1) axially mounted magnetic pick-up coils (2 cm wide, 3000 turns, 30 gauge magnetic wire), (2) photodiodes placed either so as to "see" the front face, or at the end inside tubes to "see" the rim or the flat face, (3) a ring capacitor near the front, (4) a plate capacitor at the back, and (5) ring electrodes attached directly onto the rock surface, but no strain gauges. Currents flowing from the electrodes into the rocks were measured by the voltage drop across a 2.4-M_ resistance. The grounding point was about 2/3 down the length of the cores. 200 MHz digital 4-Channel Tektronix oscilloscope was used for data acquisition.

2.2 Medium Velocity Impact Experiments

Medium velocity impact experiments were carried out at the NASA Ames Vertical Gun Range (AVGR) in a 3 m wide, 2.5 m high vacuum chamber, evacuated to ~4 mbar as described earlier (Freund, 2000). The vacuum enclosure shielded the sample from the Earth's magnetic field. The samples were 25 x 25 x 20 cm blocks of the Barre granite. The projectiles were 1/4-inch (6.3 mm) diameter Al spheres at vertical incidence. To remove adventitious electrostatic charges which the projectiles might accumulate during acceleration in or exiting from the gun barrel, the Al sphere passed through a thin, grounded Al foil.

The rock was instrumented with three types of sensors:

1. Three magnetic pick-up coils on 26 x 26 cm square wooden frames with 300 windings of 30 gauge magnet wire, one positioned 10 cm above the plane of impact to record primarily the emission from the plasma plume (Crawford and Schultz, 1991), the two other coils positioned slightly below midheight and near the bottom of the block, respectively. Though the spacing between the coils was less than their diameters, self-induction was found to be negligible.

2. Three capacitors, consisting of 22 cm long, 20 mm wide pieces of 0.05-mm-thick electrical insulation tape onto which were glued 20-cm-long, 12-mm-wide strips of Cu tape. The location of the capacitor sensors will be shown in the figures below.

3. Two electrodes made of adhesive conductive Cu tape, 20 cm long, 12 mm wide, glued directly onto the rock to provide direct contacts. The electrodes were connected to ground through 2.4-M_ resistances across which the voltage drop was measured. The location of the electrodes will be shown in the figures below.

The rock rested on a 1.5-cm-thick Al metal plate, connected to the oscilloscope ground.

For data acquisition two four-channel digital oscilloscopes were used in parallel: (1) a 200-MHz Tektronix oscilloscope, model 420A, to record the signals from the three pick-up coils and one of the two electrodes; (2) a 500-MHz Tektronix oscilloscope, model 756, to record the signals from the three capacitors and the other electrode. Data acquisition was triggered through the AVGR electronics. Both oscilloscopes stored the data from the trigger point minus 5 ms until the buffer was full, typically ~30 ms after impact.

All shots were fired at normal incidence. Shots 1 and 3 served to test all channels and tune the settings so that the signals recorded by each sensor were strong enough and clearly resolved but not off-scale. Shot 2 was lost due to a triggering error. Shot 4 at 1.46 km/s produced usable data on all eight channels, while shot 5 at 1.79 km/s gave usable data on five of the eight channels. The shots, all fired at the same spot, led to the excavation of a near-cylindrical hole, ~10 mm wide, growing to a depth of ~50 mm and possibly deeper after shot 5. Shot 6 at 4.45 km/s gave usable data on all eight channels but caused three fissures to appear at roughly 120° on the surface of the block. Shot 7 at 5.64 km/s caused catastrophic fracture into three segments.

2.3. Samples

The low-velocity experiments were conducted with two rocks, air-dry: (1) a whitish-gray speckled gabbro with phaneritic texture containing ~80% whitish plagioclase (bytownite with 88% An) and ~20% large, dark, elongate pyroxene (clinopyroxene « orthopyroxene) with thin augite exsolution lamellae, and (2) a dark, almost black diorite with phaneritic texture containing abundant ortho-pyroxene, often with very fine exsolution lamellae, clouded plagioclase (labradorite with 67% An), magnetite, minor hornblende and biotite and very minor K-feldspar and quartz. When impacted several times, the gabbro cores chipped more easily than the diorite cores.

The medium-velocity experiments were conducted with air-dry granite from Barre, Vermont, rough-cut with a diamond saw but not polished. The granite is coarse-grained, light gray with approximately 35% quartz, 55% sodium and potassium feldspar, minor plagioclase, plus some biotite and hornblende. The rock shows no sign of texture that could lead to a preferred orientation of its quartz crystals.

3. Results

3.1. Low-Velocity Impacts

When a steel ball hits the rock, several effects occur in rapid succession, variable from shot to shot, but displaying a recurring pattern. Figure 1a shows an experiment with a gabbro core, equipped with a photodiode at the front face (channel 4), a ring capacitor near the front (channel 2), and a plate capacitor at the back end (channel 3).

The moment of impact is marked by a short (10 μs), weak light blip (vertical arrow). About 150 μs after impact the ring capacitor, 10 mm from the impact point, begins to record a positive voltage that rises to above +400 mV. About 250 μs after impact the back end plate capacitor, 70 mm from the impact point, begins to show a positive voltage that rises to +40 mV. When the front ring capacitor voltages exceeds +400 to +450 mV (~450 μs after impact), light is emitted, much stronger and longer lasting than that at impact. This effect will be called the "delayed light." At the same moment the front capacitor voltage breaks down and may even go negative.

The same effects are even more clearly displayed in Figure 1b where a diorite core was used. Only the front capacitor voltage (channel 3) and the light emission (channel 4) are shown. The impact light blip was not picked up, probably because the ricocheting steel ball blocked the light path. The dotted line on channel 3 traces the voltage at the front capacitor that may have reached values well above +400 mV without the intervening delayed light emission, causing it to break down abruptly. As in Figure 1a, when the delayed light emission occurs, the front capacitor voltage collapses and turns briefly negative. It recovers to around +300 mV and decays in an irregular manner that may contain some low frequency components.

In Figure 1c, also with the diorite core, the front ring capacitor was replaced by a magnetic pick-up coil, while leaving the photodiode at the front and the plate capacitor at the end in place. At impact, the coil registers an EM emission. Its intensity increases slightly at the delayed light emission. This is a recurring feature that is often observed and some times quite pronounced.

In Figure 2 the magnetic pick-up coil (channel 2) was moved along the axis and a contact ring electrode (channel 1) was installed at the front end, leaving the back end plate capacitor in place. Channel 3 records the back end capacitor voltage. Channel 4 records the light emission. What is different with respect to the configurations in Figures 2a-2c is that the rock core now is grounded at two places, first via the electrode across the 2.4-M_ resistor and second at the grounding point about 2/3 down the length of the core. At impact, a 10-20 μs light blip occurs plus a sharp onset of EM emission that continues for several ms. The front end electrode records a positive voltage ~200 μs after impact, indicating that the electrode begins to inject electrons into the rock. The electron injection increases steeply with the voltage signal rising beyond +500 mV and eventually going off scale. The

delayed light emission sets in sharply 400-420 μs after impact. At the same moment the positive voltage recorded by the back end capacitor (which had just started to rise) begins damped oscillations in the range of 8 kHz.

Such kHz oscillations at the back end capacitor are seen in all experiments where the rock was grounded at more than one place. Examples are given in Figures 4a and 4b with a diorite core equipped with three ring electrodes in direct contact with the rock surface (channels 1-3), the back end capacitor, and the front photodiode. Because only four recording channels were available, we conducted two shots under otherwise identical conditions, switching channel 4 from the back capacitor (Figure 3a) to the photodiode (Figure 3b).

In Figure 3a the moment of impact is moved off-scale to the left. The three electrode voltages rise simultaneously, indicating the time when all three electrodes begin to inject electrons into the rock. As the voltage at the first two electrodes reaches maximum and begins to break down (presumably because of the on-set of a delayed light emission), the voltage of the back end capacitor begins to oscillate at about 40-45 kHz, which is higher than in the case depicted in Figure 2. The oscillations decay over <1 ms. Concurrently, a 40-45 kHz ripple appears on the voltage signal recorded from the third electrode, closest to the grounding point, suggesting some kind of coupling between the electron injection and the electric field at the rock surface sensed by the back end capacitor.

The second shot is depicted in Figure 3b where channel 4 was used for the photodiode. A 20-30 μs impact light blip is clearly identified. It is followed 250 μs later by the simultaneous build-up of the voltage at the three contact electrodes, signaling electron injection into the rock. About 400 μs later a sudden, intense delayed light emission occurs. At this exact moment, the voltage at the first and second electrode voltage begins to break down. The third electrode, closest to the grounding point, registers the same faint 40-45 kHz ripple as in Figure 3a. This indicates that when the rock is grounded and a positive charge appears on its surface, electron injection occurs, often in an oscillatory fashion. This effect will be more clearly demonstrated in the course of the medium velocity experiments. The ensemble of the results obtained so far suggest that the low-velocity impacts, even those with the lightest steel balls, generate electrical charge carriers in the rocks. Their sign is positive. There seems to be no threshold for the appearance of these charge carriers, though the range of the kinetic energy deposited into the rocks in this part of the impact experiments, 0.06-0.4 Joules, is small and may have precluded identification of such a threshold. Furthermore, the observations indicate that the charge carriers spread through the cores at a relatively high speed, in the range of 100-300 m/s. Such high speed can only be associated with electronic charges, and since they carry a positive sign, they are identified as defect electrons.

When the integrated visible light intensity as registered by the front end photodiode is plotted versus the kinetic energy of impact, a linear relationship seems to be obtained as demonstrated in Figure 4. This is consistent with the idea that the volume in which PHPs are activated and, hence, the number of positive hole charge carriers generated increase linearly with impact energy.

Another experiment was set up to test whether the rock becomes conductive as the cloud of charge carriers propagates. The sample consisted of a rectangular piece of diorite, 15 x 15 x 40 mm, with polished ends onto which 5-mm-diameter gold electrodes were sputtered; 25 V were applied across the long dimension, 40 mm, while the block was impacted from the side, normal to the applied electric field, using a 1/8-inch steel ball. The current flowing through the rock was determined by measuring the voltage drop across a 2.4-M_ resistance R (Channel 3). In addition, the light emission the front face and the EM emission were recorded (channel 1 and channel 4, respectively).

A sharp onset of EM emission marks the impact as seen in Figure 5. About 150 μs later, the voltage across the resistance R rises, indicating a current flowing through the rock, reaching 300 mV within 150 μs, and ending abruptly with a sharp light pulse accompanied by a <10 μs long EM pulse. Within 200 μs the sign of the voltage reverses, indicating a reversal of the current. Thereafter, both voltage signals

and EM signals reverberate for a few milliseconds. These observations suggest that the charge carriers generated locally by the impact propagated outward from their source volume, causing the rock to become momentarily conductive and to support a cross current between the Au electrodes.

3.2. Medium-Velocity Impacts

With the medium velocity impacts three questions were addressed: (1) Will the granite also generate positive hole charge carriers? (2) Is the mode of activation different at high kinetic energies? (3) How does the presence of piezoelectric quartz affect the measurements?

Figure 6 shows data recorded on the 200-MHz oscilloscope during shot 4 (1.46 km/s). The locations of the coils and the top contact electrode are indicated in the inset. The approximate time of impact is marked by the dotted line. Channels 1-3 registered signals from the top, middle and bottom pick-up coils at 200, 100, and 50 mV/div, respectively. Channel 4 registered the signal from the top contact electrode at 200 mV/division.

All three coils "see" an EM emission. The signal recorded by the plasma coil is relatively weak and lasts for less than 500 μs, suggesting that the impact did not produce the type of intense plasma plume known from high velocity or hypervelocity impacts (Crawford and Schultz, 1991). The EM signal recorded by the middle coil lasts about 500 μs and that recorded by the bottom coil for about 1.5 ms.

Figure 7a shows the same EM signals as in Figure 6 at higher time resolution. Taking the first EM spike recorded by the plasma coil as the moment of impact, the middle coil and bottom coil begin registering EM emissions at the times as marked by the arrows, about 35 μs and 65 μs after impact. The delayed onset indicates that the middle and bottom coils register an electric charge moving through the block much faster than after the low velocity impact experiments, i.e. at a speed commensurate with the velocities of the P or S waves, about 6 and 3.4 km/sec respectively.

The same ~35 and 65 μs delay of the signals from the middle and bottom coils was observed during shot 6 at 4.45 km/s as shown in Figure 7b, indicating that the time delay is not a function of the impact velocity. The envelope of the plasma EM emission signal is quite regular, possibly because the previous shots had by then excavated a hole ~10 mm wide and 70 mm deep into the granite block which focussed the plasma plume into a narrow fountain. Shot 6 resulted in three vertical fissures, running through the granite block at ~120° with respect to each other. These fissures began to form after the 2 ms time window presented in Figure 7b. However, they did not yet lead to a disintegration of the block.

An example of EM emission when the rock fractures after the impact is shown in Figure 7c, presenting data from shot 7 at 5.64 km/s. The block broke into three sections along the fissures preformed during shot 6. The data from the bottom coil were lost. The EM emission recorded by the plasma coil and the middle coil is shown on two different timescales, over 30 ms in the main panel and over 2.5 ms in the inset. The plasma coil registered an intense EM emission immediately after impact with reverberations that lasted for about 2 ms, maybe because the plasma jet emitted upon impact became entangled in the cracks that opened as the rock began to disintegrate. The middle coil registered its first signal with the expected time delay of ~65 μs, followed by multiple bursts of EM emission, at 5, 20, and 26.5 ms, probably all associated with the opening and propagation of the cracks.

While the EM emissions recorded by the pick-up coils indicate rapidly moving charges generated upon impact, the three capacitive sensors register the potential appearing on the granite surface. Figure 8a shows the voltage response of the three capacitive sensors that were all on one side of the block as depicted in the inset plus the voltage registered by the bottom electrode, <1 cm from the grounded metal base. The time of impact is marked by the dotted line.

The response of the capacitive sensors is significantly different from that seen after low velocity impacts. Now, the signals travel much faster, arriving within 65 μs or less at the three sensor locations ~15, 18, and 25 cm from the point of impact, respectively. However, instead of a smoothly rising

positive voltage as before, the signals begin with a sequence of short pulses, lasting for 20-30 μs. After ~500 μs, e.g. at a time when the EM emissions have largely ended as shown in Figure 7a, a strong positive charge builds up on the entire rock surface. Concurrently, a new kind of oscillations takes over, their amplitudes increasing from the top to the bottom capacitive sensors.

In Figure 8b the rapid pulses during the first 500 μsec after impact are replotted. The vertical line marks the time of impact as derived from the onset of the EM emission as seen by the plasma coil (Figure 7a). The inset in the upper right shows the P and S wave velocity for Barre granite as a function of confining pressure (Christensen, 1982). In vacuum, the P and S wave velocities should all into the range of 5.5-6 km/s and 3-3.4 km/s, respectively.

Because the granite contains quartz, the propagation of the P and S waves should be accompanied by transient piezoelectric voltage effects. Indeed, shortly after impact, all three capacitive sensors begin to register a series of short voltage pulses, 20-30 μs wide. The distances from the point of impact to the three 20-cm-long, 1-cm-wide capacitor stripes vary from 12.5 to 17 cm (average ≈15 cm) for the top sensor, from 15 to 23 cm (average ≈19) for the middle sensor, and from 22 to 31 cm (average 27 cm) for the bottom sensor. The arrival times of the first voltage pulse at the three sensor locations are delayed by ~20-30, 30-40 and 50-65 μs, respectively.

These delays suggest a wave traveling down through the rock at a speed close to that of the P wave, at about 6 km/s. The signals, in particular those from the top and middle sensors, show a rapid inversion from positive to negative voltages such as one would expect from the compression and rarefaction phases of a passing P wave. Marking this first train of voltage pulses by solid circles, the solid line in Figure 8b traces the propagation of the P wave. Beginning with the second voltage pulse registered by the top sensor, a second line (dashed) can be drawn through a second, slower train of voltage pulses that appears to correspond to the S wave propagating at about 3 km/s. Finally, the open circles and dotted lines in Figure 8b tentatively mark signals that may be caused by the reflected P and S waves.

If these trains of voltage pulses recorded by the three capacitive sensors are indeed due to a piezoelectric response from quartz at the rock surface, these signals should last only as long as the transient stresses exerted by the traveling P and S sound waves. Therefore, the piezoelectric signals should rapidly decay. Assuming that the sound waves reverberate in the granite block over two to three reflection cycles, each lasting <100 μs for the P wave and <200 μs for the S wave, the piezoelectric signals are expected to decay within 500-700 μs. This time window agrees rather well with the duration of the EM emission recorded by the middle coil as shown in Figures 8a and 8b, suggesting that a large component of the EM emission comes from transient piezoelectric voltage pulses that are created by the reverberating P and S waves.

However, Figure 8a also shows that, while the piezosignals fade away within 700-800 μs after impact, the top capacitive sensor continues to register a positive potential that builds up over the same time, indicating a positive surface charge. The potential reaches about +400 mV within 700-800 μs and decays over the next 2 ms. The middle and the bottom capacitive sensors register +380 mV and +300 mV, respectively. These voltages are overprinted by amplitude variations that become more intense from top to bottom and are in phase.

Overall, with some additional features and complications, the medium-velocity impacts yield voltage signals that resemble those recorded after the low-velocity impacts. In both cases there is evidence that positive charge carriers are generated or activated by the impacts or rather by the acoustic waves resulting from the impact events. In the case of low-velocity impacts the charge generation seems to be limited to a small rock volume close to the impact point. From there the charges propagate as a cloud through the rock volume. In the case of the medium-velocity impacts the higher kinetic energy carried by the impactors produce sound waves of higher amplitudes. Apparently, after the reverberations of the sound waves had died down, the entire rock volume was left with activated positive holes which

then spread outward toward the surface to reach a new equilibrium before deactivating, probably by some recombination or trapping mechanism.

The amplitudes of the oscillations that overprint the capacitive voltage signals increase the closer the sensor is to the grounded metal base plate. The oscillations are in-phase, suggesting that they are due to electric field variations occurring simultaneously at all three sensor locations. By contrast, the oscillations of the capacitive sensors are out-of-phase with those of the contact electrodes. The question arises: What is the cross relationship between these two sets of signals?

Figure 9 plots the voltage of the bottom capacitive sensor and voltage of the bottom contact electrode, the former representing the surface potential and the latter deriving from the current injected into the rock. As seen in the insets in Figure 8, both sensors are close to the grounded metal base plate, ~1 cm, but on opposite sides of the block. The oscillations are mostly out-of-phase, especially from 1 ms onward, suggesting that, when the potential at the rock surface exceeds the barrier height, the contact electrode will begin injecting electrons. This in turn causes the potential at the rock surface to break down, shutting off the electron injection. As long as positive holes still arrive at the surface from within the bulk, the potential recovers. However, as the process slows down, the frequency of the oscillations decreases. Eventually, when the surface potential can no longer reach or exceed the barrier height, electron injection shuts off entirely.

4. Discussion

Low- and medium-velocity impact experiments seem to be a valuable tool to study the activation of charge carriers in rocks. Through timing the impacts and measuring the evolving processes with microsecond to millisecond resolution, the response of rocks can be studied in ways that are not possible with rock samples placed under slowly increasing compressive or shear stress. The insights gained may shed light on a range of phenomena associated with earthquake activity – electrical, electromagnetic, and luminous – that have a long tradition in folklore from many parts of the world and have been reported in the scientific literature.

4.1. Recapitulation

When common igneous rocks are subjected to the sudden stress load of an impact, they generate highly mobile charge carriers. The charge carriers are electronic in nature. They spontaneously appear upon impact, propagate and disappear after a few milliseconds. They can be reactivated by repetitive impacts. Apparently, these charge carriers already exist in the rocks in their "as received" state, albeit in an electrically inactive, dormant form. At low kinetic impact energy they are activated in a small volume close to the impact point. At higher kinetic impact energies they seem to be activated in the wake of the sound waves, filling momentarily the entire rock volume.

Since the charge carriers are electronic in nature and positive, they can only consist of holes as argued in section 3, specifically of positive holes, e.g. defect electrons in the O 2p-dominated valence band of the constituent silicate minerals, which are equivalent to O^- in an O^{2-} matrix. A likely dormant precursor form are positive hole pairs, PHPs, chemically equivalent to peroxy links, O^-–O^- or $O_3X/^{OO}\backslash XO_3$ with X = Si^{4+}, Al^{3+}, etc. The PHPs are believed to be introduced into nominally anhydrous minerals through the dissolution of small amounts of H_2O and subsequent redox conversion of O_3X-OH pairs into $O_3X/^{OO}\backslash XO_3$ plus H_2 as described by equations (1)-(4).

4.2. Why have they not been observed earlier?

On the basis of the available impact data all three types of rocks – gabbro, diorite and granite – display a behavior that is consistent with the activation of positive hole charge carriers. At the same time these

rocks are good insulators when dry and at ambient temperature. Their electrical conductivity has been studied under a wide variety of conditions: temperature, atmosphere, confining pressure etc. (e.g. Shankland and Ander, 1983). However, none of these studies, though carefully conducted, seem to have produced evidence for the highly mobile electrical charge carriers that show up so prominently in the impact experiments described here.

This is reminiscent of a situation encountered during a study of the model insulator MgO and its electrical conductivity as a function of temperature (Freund et al., 1993). MgO had long been considered an excellent insulator up to temperatures above 700°C, the onset of ionic conductivity. There were hints of an unusual orders-of-magnitude increase in conductivity in the 400-700°C interval but those hints were not pursued because it could be demonstrated that the enhanced conductivity was confined to the surface. It looked suspiciously like some sort of contamination or "dirt." Indeed, upon heating MgO crystals long enough to temperatures well above 700°C, the enhanced surface conductivity can be shown to disappear, suggesting that the contamination or "dirt" had been successfully removed. This settled the question for good in the minds of most investigators. A similar orders-of-magnitude enhancement of the electrical conductivity below 700°C was observed during the study of single crystals of upper mantle olivine by Constable and Duba (1990). As in the case of MgO, the conductivity seemed confined to the crystal surface. Upon prolonged heating in a 1:1 CO/CO_2 gas mixtures, the enhanced conductivity disappeared, leading to the suggestion that a thin but conductive carbon film had vapor-deposited on the sample surface from the CO/CO_2 gas.

Meanwhile evidence had accumulated that MgO and probably also olivine crystals from the upper mantle contain peroxy anions and peroxy links respectively, e.g. PHPs, that are capable of releasing positive hole charge carriers (King and Freund, 1984; Freund et al., 1993; 1994). The behavior of these positive holes is unlike that of other charge carriers and unlike that expected for carbon films. The property that is most easily misunderstood is due to the mutual repulsion of positive holes in the bulk which effectively "pushes" them to the surface, causing an enhanced surface conductivity. However, positive holes are nothing but O^- in an O^{2-} matrix and therefore highly oxidizing radicals. Their behavior, i.e. their chemical reactivity during a conductivity experiment chemical reactivity needs to be taken into account. Allowing positive hole charge carriers at a surface to react with CO/CO_2 gas mixtures at 700°C leads to their annihilation, $CO + 2\ O^- = CO_2 + O^{2-}$. Using the reaction $CH_4 + O^- = \bullet CH_3 + OH^-$, where $\bullet CH_3$ represents the gas-phase methyl radical, the O^- can in fact be titrated off the sample surface. Because of these unusual physical and chemical properties of the positive holes outlined above their potentially very important role as charge carriers in rocks has not been recognized, despite of many careful laboratory studies.

4.3 Positive Holes and Electron Injection

In the case of low velocity impacts, the activation seems to be confined to a small volume near the impact point. The light blip marking the time of impact is probably due to triboluminescence, coming from electron-hole pairs generated by rapidly moving dislocations and their radiative recombination. From the small source volume the positive holes propagate outward as a charge cloud, causing positive potentials, EM and delayed light emission.

In the case of medium velocity impact experiments, the activation of positive hole charge carriers most likely occurs in the wake of the P or S waves. After the initial piezoelectric signals from quartz crystals that were stressed by the propagating P and S waves have died down, the capacitive sensors register a pervasive positive charge that persists for ~3 ms, while the contact electrodes indicate pulses of electrons flowing into the rock.

Figure 10 sketches the sequence of events following a medium velocity impact with special emphasis on the surface potential recorded by the capacitive sensors and the current measured by the contact electrodes. In (a) the impact occurs, sending acoustic waves into the rock. In (b) positive holes, symbolized by dots, become momentarily activated in the entire rock volume. In (c), due to mutual repulsion, the positive holes diffuse outward toward the surface as indicated by the arrows. In (d) the positive potential that builds up at the surface leads to the injection of electrons, e', from the grounded metal base plate and the contact electrodes.

Figure 11 follows the evolution of the signals in greater detail. Figure 11 (top) shows the granite block with the bottom capacitive sensor recording the voltage V and the bottom electrode recording the current I near the grounded base plate. On the left the initial state is depicted, assuming that after passage of the acoustic waves, the rock volume is uniformly filled with mobile positive hole charge carriers. The initial state evolves toward the final state depicted on the right where the positive holes have come to the surface forming a positively charged surface layer balanced by a negatively charged interior. If the speed of propagation of the positive holes is of the order of 100 m/s, a block of granite measuring 25 x 25 x 20 cm can be expected to reach the final state within ~1-2 ms, as indeed observed.

The three panels in Figure 11 (middle) depict from top to bottom: (1) the surface potential as it would be expected to build up during the transition from initial to final state if the granite block were electrically isolated; the dashed line at V_i marks the threshold voltage above which electron injection can occur across the metal-to-insulator contact; (2) the surface potential as recorded by the capacitive sensor, and (3) the injection current as recorded by the contact electrode. Each time the surface potential reaches the threshold value of V_i, electron injection occurs and the potential breaks down. This in turn shuts off the electron injection and allows the surface potential to recover. As the final state is approached, the time needed to reach V_i becomes longer, causing the oscillations to slow down. In Figure 11 (bottom) the frequency of oscillation (in kHz) for the surface potential (circles) and for the injection current (squares) is plotted versus time. The frequency decreases. After ~3 ms the oscillations ceased altogether, suggesting that the positive holes reaching the rock surface no longer build up a sufficiently high potential for electron injection to occur.

4.4. Application to Electrical Phenomena Related to Earthquakes

As indicated at the beginning, the experiments reported here were not set up to simulate specific conditions encountered in connection with earthquake activity. Rather, they were designed to test whether igneous rocks such as gabbro, diorite and granite contain dormant charge carriers, which can be activated by microfracture and seismic waves.

On the basis of earlier work quoted above with laboratory-grown MgO crystals and minerals like olivine it was already known that the charge carriers which we expected to see in rocks would be positive holes that exist in an electrical inactive, dormant state, as positive hole pairs, PHPs, chemically equivalent to peroxy links, $O_3X/^{OO}\backslash XO_3$. As defect electrons in the O 2p-dominated valence band of the silicate minerals, chemically O^- in an O^{2-} matrix, such positive holes should be capable of propagating through rocks over macroscopic distances with little apparent scatter or attenuation at grain boundaries.

Most relevant to earthquake-related phenomena is the observation that the PHPs can indeed be activated by steel balls impacting at a relatively low velocity and depositing 0.06 J or less in kinetic energy. The electrical, EM, and luminous signals produced suggest that the positive hole charge carriers propagate in a specific manner through the rocks. Examples are given in Figure 1a and Figure 2. The threshold for the generation of these charge carriers seems to be so low that the crackle of microfracturing in a rock volume under increasing stress is likely to have the same effect. Therefore, as microfractures open and close in rapid succession throughout such a rock volume, they emit acoustic

wavelets. Each microfracture would generate positive holes, locally on a small scale, but in sum they would add up to a large charge cloud.

Molchanov and Hayakawa (1998a/b) introduce the concept of "electrification" by microfracturing as a possible mechanism for low-frequency EM emissions before earthquakes. The experiments described here provide a physical basis for such an "electrification". If microfractures open and close in different parts of the rock volume in rapid succession, each generating a cloud of positive holes, fluctuations in the charge carrier density are expected to produce current pulses, possibly propagating in different directions, generating a wideband EM noise and discrete pulsations as observed during the December 7, 1988, M_S=7 Spitak, Armenia, earthquake (Kopytenko et al., 1993).

With the knowledge now available that positive holes may be generated in rocks we can go one step further and address the phenomenon of earthquake lights. Reported in folklore (Tributsch, 1983), many times in the scientific literature (Derr, 1973), and photographed during the 1966 Matushiro earthquake, Japan (Derr, 1986), earthquake lights have remained a contentious issue. The reason is that no mechanism was known that could reasonably explain electric discharges at the rock-to-air interface and the appearance of "St. Elmo's fire." Neither piezoelectricity from quartz-bearing rocks (Finkelstein et al., 1973) nor sonoluminescence (Johnston, 1991) nor a fluid-driven dilatancy model (Nur, 1974) nor spray electrification by water that explosively evaporate out of the faults during a large magnitude earthquake (Lockner et al., 1983) seem to provide physical explanations for these luminous phenomena.

When positive hole clouds generated in the crust expand and reach the surface-to-air interface with its dielectric contrast, theory predicts (King and Freund, 1984) and the observations reported here confirm the appearance of surface potentials in the range of a few hundred mV. Since the charge layer built from within the rock volume is very thin, of the order of a few hundred Ångstrøm, the associated electric fields will be very high. For a charge carrier density of 10 ppm (10^{17} cm^{-3}) the thickness of the charge layer at an interface with a dielectric contrast of 10 is 1000 Å with a surface potential of the order of 400 mV (King and Freund, 1984). This translates into an electric field across the flat surface of the order of 400,000 V cm^{-1}. At rims and edges the electric field will be even higher and enough to cause dielectric breakdown of the air, corona discharges, light emission, and attendant bursts of EM radiation.

The photographs of earthquake lights during the 1966 earthquake swarm at Matsushiro, Japan, show the hilltops illuminated (Derr, 1986). This is consistent with an electric discharge where the electric fields are highest. In view of what we have learned through the impact experiments described here, it appears plausible that the charge carriers responsible for the earthquake lights during the 1966 Matsushiro event and on other occasions might have been positive holes, activated by the seismic waves.

A number of open questions remain. For instance, we have no quantitative data yet on the magnitude of the currents generated by the impacts nor the density of the positive holes activated at a given set of experimental parameters. Preliminary data on the concentration of PHPs suggest that in a typical igneous rock such as the Barre granite as much as 0.1 – 1% of all oxygen anions may be oxidized to the O^- state. This means that, if all PHPs were activated, the positive hole density would reach values as high as 10^{19}-10^{20} cm^{-3}. Theoretically (King and Freund, 1984) charge carrier densities of the order of 10^{17} cm^{-3} are enough to cause flat surface electric fields of the order of 400,000 V cm^{-1}, suggesting that activation of 1/100 to 1/1000 of the available PHPs would suffice to cause corona discharges at the rock surface.

We also don't know yet what the effect of water would be on the magnitude of the reported phenomena. However, having demonstrated that positive hole charge carriers exist in common igneous rocks opens a door to a new interpretation of electric, electromagnetic and luminous phenomena linked

to earthquake activity, regardless whether water attenuates them as they propagate through a rock, leaves them unaffected or maybe even facilitates their passage.

5 Acknowledgments.

This work was performed without formal funding support. My thanks go to Jerome G. Borucki (NASA Ames Research Center) for his early involvement in sample preparation and data acquisition, to Michael Brunetti (California Monument, Inc.) and Michael J. Causi (Cañada Marble and Granite) for cutting rocks, to Bruce W. Fouke (University of Illinois at Urbana-Champaign) for petrographic analyses, and J. Thomas Dickinson (Washington State University) for constructive criticism at a crucial time of the experiments. Peter H. Schultz (Brown University) generously provided access to the NASA AVGR. Kraig Moll (Tektronix Instruments) made the 4-channel 500 MHz oscilloscope available for the week of medium velocity impact experiments. Scott Hubbard and Douglas O'Handley (both NASA Ames Research Center) provided help through the NASA Ames Astrobiology Academy. Alexander S. Bradley (Harvard University and participant in the Astrobiology Academy 1998 Summer program) contributed to the data analysis. As reviewer, Stephen Park (University of California, Riverside) provided constructive criticism that helped improve the manuscript.

VI References

Bernabé, Y., Streaming potential in heterogenous networks, 1998. J. Geophys. Res., 103, 20,827-20,841.

Bernard, P., Plausiblity of long distance electrotelluric precursors of earthquakes, 1992. J. Geophys. Res., 97, 17,531-17,546.

Bilichenko, S.V., F.S. Iljin, and E.F. Kim, ULF response of the ionosphere for earthquake preparation processes, 1990. Dokl. Acad. Nauk USSR, 311, 1077-1080.

Bishop, J.R., 1981. Piezoelectric effects in quartz-rich rocks, Tectonophys., 77, 297-321.

Bolt, B.A., 1988. Earthquakes, W. H. Freeman and Company, New York.

Brady, B.T., and G.A. Rowell, 1986. Laboratory investigation of the electrodynamics of rock fracture, Nature, 321, 488-492.

Chmyrev, V.M., V.N. Isaev, S.V. Bilichenko, E.P. Trushkina, and G. Stanev, 1986. Electric fields and hydromagnetic waves in the ionosphere above an earthquake center, Geomagnetizm i Aeronomiia, 26, 1020-1022.

Christensen, N.I., 1982. Seismic velocities, in Handbook of Physical Properties of Rocks, pp. 1-228, CRC`, Baton Rouge, FL.

Constable, S., and A. Duba, 1990. Electrical conductivity of olivine, a dunite and the mantle, J. Geophys. Res., 95, 6967-6978.

Crawford, D.A., and P.H. Schultz, 1991. Laboratory investigations of impact-generated plasma, J. Geophys. Res., 96, 18,807-18,817.

Davis, K., and D.M. Baker, Ionospheric effects observed around the time of the Alaskan earthquake of March 28.1964, 1965. J. Geophys. Res., 70, 2251-2253.

Derr, J.S., 1973. Earthquake lights: a review of observations and present theories, Bull. Seismol. Soc. Amer., 63, 2177-21287.

Derr, J.S., 1986. Luminous phenomena and their relationship to rock fracture, Nature, 321, 470-471.

Dickinson, J.T., L.C. Jensen, M.R. McKay, and F. Freund, 1986. The emission of atoms and molecules accompanying fracture of single-crystal magnesium oxide, J. Vac. Sci. Technol., 4, 1648-1652.

Dobrovolsky, I.P., N.I. Gershenson, and M.B. Gokhberg, 1989. Theory of electrokinetic effects occurring at the final stage in the preparation of a tectonic earthquake, Phys. Earth Planet. Int., 57, 144-156.

Draganov, A.B., U.S. Inan, and Y.N. Taranenko, 1991. ULF magnetic signatures at the Earth surface due to ground water flow: a possible precursor to earthquakes, Geophys. Res. Lett., 18, 1127-1130.

Drobgev, V.I., V.M. Krasnov, and R.M. Salihov, 1978. About ionospheric perturbation associated with earthquake and explosions, Izv. Vyssh. Uchebn. Zaved., 21, 1862-1978.

Edwards, A.H., and W.B. Fowler, 1982. Theory of the peroxy-radical defect in a-SiO_2. Phys. Rev. B, 26, 6649-6660.

Eiby, G.A., 1980. Earthquakes, Van Nostrand Reinhold Company, New York, NY.

Emmermann, R., and J. Lauterjung, 1997. The German continental deep drilling program KTP: Overview and major results, J. Geophys. Res., 102, 18,179-18,201.

Enomoto, Y., and H. Hashimoto, 1990. Emission of charged particles form indentation fracture of rocks, Nature, 346, 641-643.

Finkelstein, D., U.S. Hill, and J.R. Powell, 1973. The piezoelectric theory of earthquake lightning, J. Geophys. Res., 78, 992-993.

Fraser-Smith, A.C., A. Bernardi, P.R. McGill, M.E. Ladd, R.A. Helliwell, and O.G. Villard, 1990. Low-frequency magnetic field measurements near the epicenter of the Ms=7.1 Loma Prieta earthquake, Geophys. Res. Lett., 17, 1465-1468.

Freund, F., 2000. Time-resolved study of charge generation and propagation in igneous rocks J. Geophys. Res. 105, 11,001-11,019.

Freund, F., and J.G. Borucki, 1999. Charge carrier generation and charge cloud propagation following 100 m/s impacts on igneous rocks, in Atmospheric and Ionospheric Electromagnetic Phenomena Associated with Earthquakes, edited by M. Hayakawa, pp. 839-857, Terra Sci. Publ., Tokyo.

Freund, F., M.M. Freund, and F. Batllo, 1993. Critical review of electrical conductivity measurements and charge distribution analysis of MgO, J. Geophys. Res., 98, 22,209-22,229.

Freund, F., and M.M. Masuda, 1991. Highly mobile oxygen hole-type charge carriers in fused silica, J. Mater. Res., 8, 1619-1622.

Freund, F., and H. Wengeler, 1982. The infrared spectrum of OH--compensated defect sites in C-doped MgO and CaO single crystals, J. Phys. Chem. Solids, 43, 129-145.

Freund, F., Whang, E.-J., Batllo, F., Desgranges, L., Desgranges, C., and Freund, M.M., 1994. Positive hole–type charge carriers in oxide materials, in: Grain Boundaries and Interfacial Phenomena in Electronic Ceramics, edited by L.M. Levinson, pp. 263-278, Amer. Ceram. Soc. Cincinnati, OH

Friebele, E.J., D.L. Griscom, M. Stapelbroek, and R.A. Weeks, 1979. Fundamental defect centers in glass: The peroxy radical in irradiated high-purity fused silica, Phys. Rev. Lett., 42, 1346-1349.

Fujinawa, Y. and K. Takahashi, 1990. Emission of electromagnetic radiation preceding the Ito seismic swarm of 1989, Nature, 347, 376 – 378.

Galperin, Y.I., G. V.A., N.V. Jorjro, R.A. Kavrazhkin, Y.V. Lissakov, V.D. Maslov, L.M. Nikolaenko, R.Z. Saddeev, O.A. Molchanov, M.M. Mogilevsky, L.S. Alperovich, M.B. Gokhberg, E.A. Ivanov, O.A. Pokhotelov, H. Reme, J.M. Bosqued, C. Beghin, and J.J. Berthelier, 1985. VLF and ELF effects in the upper ionospheric caused by large-scaled acoustic waves in the lower ionosphere observed from aurol-3 satellite, Result of the ARCAD-3 Project, Cepadues, Toulouse, 661-684.

Geller, R.J., 1996. Debate on VAN, Geophys. Res. Lett., 23 (whole issue #11).

Geller, R.J., 1997. Earthquake prediction: a critical review, Geophys. J. Int., 131, 425-450.

Hadjicontis, V., and C. Mavromatou, 1994. Transient electric signals prior to rock failure under uniaxial stress, Geophys. Res. Lett., 21, 1687-1690.

Hedervari, P., and Z. Noszticzius, 1985. Recent results concerning earthquake lights, 3, 705-708.

Horn, R.G., and D.T. Smith, 1992. Contact electrification and adhesion between dissimilar materials, Science, 256, 362-365.

Huang, Q., and M. Ikeya, 1998. Seismic electromagnetic signals (SEMS) explained by a simulation experiment using electromagnetic waves, Phys. Earth Planet. Inter., 109, 107-114.

Johnston, A.C., 1991. Light from seismic waves, Nature, 354, 361.

Johnston, M.J.S., 1997. Review of electric and magnetic fields accompanying seismic and volcanic activity, Surveys in Geophysics, 18, 441-475.

Johnston, M.J.S., and M. Parrot, 1989. Seismoelectromagnetic Effects, Phys. Earth Planet. Inter., (Special Issue), 57, 1-177.

King, B.V., and F. Freund, 1984. Surface charges and subsurface space charge distribution in MgO containing dissolved traces of water. Phys. Rev., B 29, 5814-5824.

Kopytenko, Y.A., T. Matiashvili, P.M. Voronov, E.A. Kopytenko, and O.A. Molchanov, 1993. Detection of ultra-low-frequency emissions connected with the Spitak earthquake and its aftershock activity, based on geomagnetic pulsation data at Dusheti and Vardzia observatories, Phys. Earth Planet. Inter., 77, 88-95.

Kustov, V.A., and Liperovsky, 1988. About perturbations in the ionospheric F-region before strong earthquakes, Izv. Akad. Nauk USSR, Fiz. Zemli, N4, 12-20.

Larkina, V.I., V.V. Migulin, O.A. Molchanov, A.S. Ilchin, and V.V. Shvetsova, 1988. Characteristics of the excitation of low-frequency emissions in the upper ionosphere above earthquake regions, Geomagn. Aeron., 28, 685-689.

Lee, C. C., J. Y. Liu and C. J. Pan, 2000. The height of sporadic-E layer simultaneously observed by the VHF radar and ionosondes in Chung-Li. Geophys. Res. Lett. 27: 641-644.

Liu, J. Y., Y. H. Chu, M. Q. Chen, L. C. Tsai and C. M. Huang, 2000. Modeling and ground observations of the ionosphere related to the COSMIC project. Terr. Atmo. Ocean. Sci. 11: 349-364.

Loeb, I.B., 1958. Static Electrification, Springer, Berlin.

Lockner, D.A., Johnston, M.J.S., and Byerlee, J.D., 1983. A mechanism to explain the generation of earthquake lights. Nature 302, 28-32.

Martens, R., H. Gentsch, and F. Freund, 1976. Hydrogen release during the thermal decomposition of $Mg(OH)_2$ to MgO, J. Catalysis, 44, 366-372.

Masood, E., 1995. Greek earthquake stirs controversy over claims for prediction, Nature, 375, 617.

Merzer, M., and S.L. Klemperer, 1997. Modeling low-frequency magnetic-field precursors to the Loma Prieta earthquake with a precursory increase in fault-zone conductivity, Pure Appl. Geophys., 150, 217-248.

Meyer, L.L., 1977. California Quake, Sherbourne Press, Nashville, TN.

Michael, A.J., 1996. Testing prediction methods: Earthquake clustering versus the Poisson model, Geophys. Res. Lett., 24, 1891-1894.

Molchanov, O.A., and M. Hayakawa, 1998a. Subionospheric VLF signal perturbations possibly related to earthquakes, J. Geophys. Res., 103 (A8), 17,489-17,504.

Molchanov, O.A., and M. Hayakawa, 1998b. On the generation mechanism of ULF seismogenic electromagnetic emissions, Phys. Earth Planet. Inter., 105, 201-210.

Molchanov, O.A., M. Hayakawa, T. Oudoh, and E. Kawai, 1998. Precursory effects in the subionospheric VLF signals for the Kobe earthquake, Phys. Earth Planet. Interiors, 105, 239-248.

Molchanov, O.A., Y.A. Kopytenko, E.A. Kopytenko, T. Matiashvili, A.C. Fraser-Smith, and A. Bernardi, 1992. Results of ULF magnetic field measurements near the epicenters of the Spitak (Ms=6.9) and Loma Prieta (Ms=7.1) earthquakes: Comparative analysis, Geophys. Res. Lett., 19, 1495-1498.

Morat, P., and J.L. Le Mouel, 1987. Variation of the electric resistivity of large rock samples with stress, Geophysics, 52, 1424 – 1430.

Morat, P., and J.-L. LeMouël, 1992. Electrical signals generated by stress variations in porous non-saturated rocks, C.R. Acad. Sci. Ser. II, 315, 955-963.

Morrison, F.D., E.R. Williams, and T.D. Madden, 1989. Streaming potentials of Westerly granite with applications, J. Geophys. Res., 94, 12449-12461.

Nur, A., 1974. Matsushiro, Japan, earthquake swarm: Confirmation of the dilatancy-fluid diffusion model, Geology, 2, 217-221.

Oommen, T.V., 1988. Static electrification properties of transformer oil, IEEE Transaction on Electrical Insulation, 23, 123-128.

Park, S.K., 1997a. Electromagnetic precursors to earthquakes: a search for predictors, Science Progress, 80, 65-82.

Park, S.K., 1997b. Monitoring resistivity change in Parkfield, California: 1988-1995, J. Geophys. Res., 102, 24,545-24,559.

Park, S.K., M.J.S. Johnston, T.R. Madden, F.D. Morgan, and H.F. Morrison, 1993. Electromagnetic precursors to earthquakes in the ULF band: a review of observations and mechanisms, Reviews Geophys., 31, 117-132.

Pham, V.N., D. Boyer, G. Chouliaras, J.L. Le Mouel, J.C. Rossignol, and G.N. Stavrakakis, 1998. Characteristics of electromagnetic noises in Ioannina region (Greece): a possible origin for so called "Seismic Electric Signals" (SES), Geophys. Res. Lett., 25, 2229-2232.

Quellet, M., 1990. Earthquake light and seismicity, Nature, 348, 492.

Rikitake, T., 1976. Earthquake Prediction, Elsevier Sci. Publ. Co., Amsterdam.

Rossman, G.R., 1996. Studies of OH in nominally anhydrous minerals, Phys. Chem. Minerals, 23, 299-304.

Schock, R.N., and A. Duba, 1985. Point defects and the mechanisms of electrical conduction in olivine, in Point Defects in Minerals, edited by R.N. Schock, pp. 88-96, Amer. Geophys. Union, Washington, D.C.

Serebryakova, O.N., S.V. Bilichenko, V.M. Chmyrev, M. Parrot, J.L. Rauch, F. Lefeuvre, and O.A. Pokhotelov, 1992. Electromagnetic ELF radiation from earthquake regions as observed by low-altitude satellites, Geophys. Res. Lett., 19, 91-94.

Shankland, T.J., 1981. Electrical conduction in mantle materials., in Evolution of the earth, edited by R.J. O'Connell, and W.S. Fyfe, pp. 256-263, Amer. Geophys. Union, Washington, D.C.

Shankland, T.J., and M.E. Ander, 1983. Electrical conductivity, temperature and fluids in the crust, J. Geophys. Res., 88, 9475-9484.

Tributsch, H., 1983. When Snakes Awake: Animals and Earthquake Prediction, MIT Press, Cambridge, Mass.

Varotsos, P., N. Sarlis, M. Lazaridou, and P. Kapiris, 1997. Transmission of stress induced electric signals in dielectric media, J. Appl. Phys., 83, 60-70.

Yoshida, S., O.C. Clint, and P.R. Sammonds, 1998. Electric potential changes prior to shear fracture in dry and saturated rocks, Geophys. Res. Lett., 25, 1577-1580.

Yoshida, S., M. Uyeshima, and M. Nakatani, 1997. Electric potential changes associated with slip failure of granite: Preseismic and coseismic signals, J. Geophys. Res., 102, 14,883-14,897.

Zhijia, Z., 1989. Investigation of tectonomagnetic phenomena in China, Phys. Earth Planet. Int., 57, 11-22.

Figures

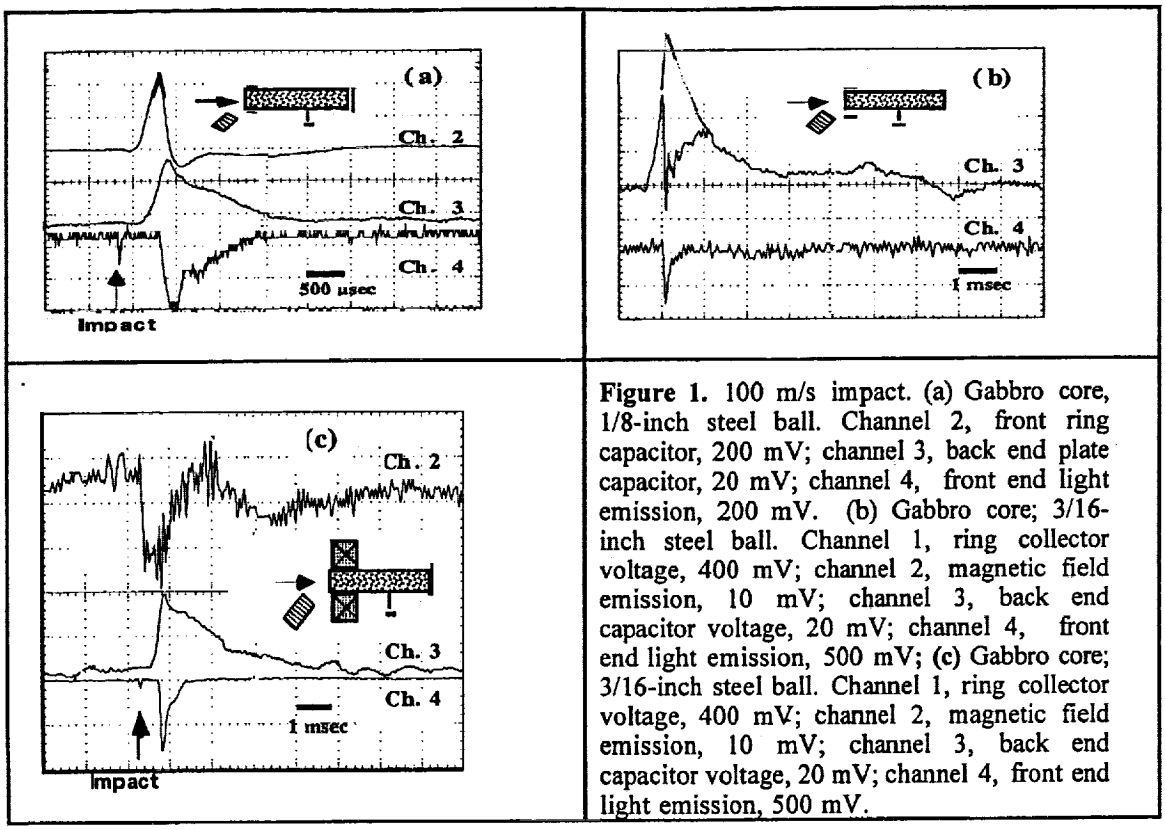

Figure 1. 100 m/s impact. (a) Gabbro core, 1/8-inch steel ball. Channel 2, front ring capacitor, 200 mV; channel 3, back end plate capacitor, 20 mV; channel 4, front end light emission, 200 mV. (b) Gabbro core; 3/16-inch steel ball. Channel 1, ring collector voltage, 400 mV; channel 2, magnetic field emission, 10 mV; channel 3, back end capacitor voltage, 20 mV; channel 4, front end light emission, 500 mV; (c) Gabbro core; 3/16-inch steel ball. Channel 1, ring collector voltage, 400 mV; channel 2, magnetic field emission, 10 mV; channel 3, back end capacitor voltage, 20 mV; channel 4, front end light emission, 500 mV.

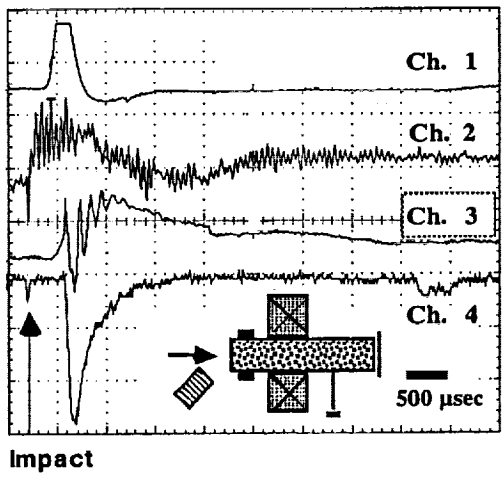

Figure 2. A 100 m/s impact. Diorite core; 3/16-inch steel ball. Channel 1, ring electrode voltage, 400 mV; channel 2, EM emission, 10 mV; channel 3, back end capacitor voltage, 20 mV; channel 4, front end light emission, 500 mV.

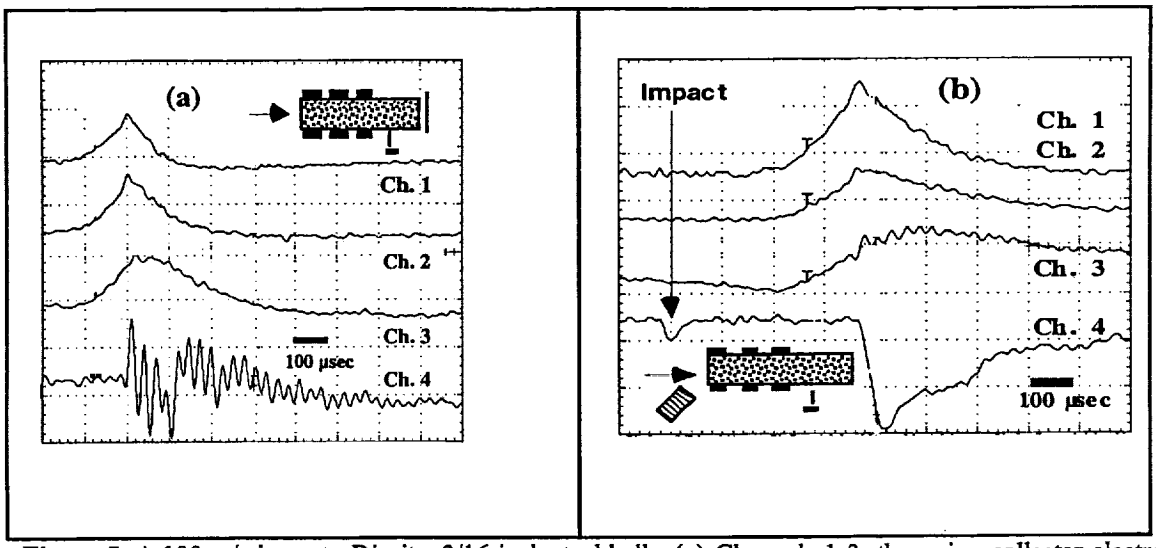

Figure 3. A 100 m/s impact. Diorite, 3/16-inch steel balls. (a) Channels 1-3, three ring collector electrodes, 500 mV, 100 mV and 20 mV, respectively; channel 4, back end capacitor voltage, 5 mV. Note the kilohertz oscillations of the back end capacitor voltage and the 38-kHz ripple on the three ring collectors after the onset of the light emission; (b) Channels 1-3, three ring collector electrodes, 500 mV, 100 mV and 20 mV, respectively; channel 4, front end light emission, 1 V.

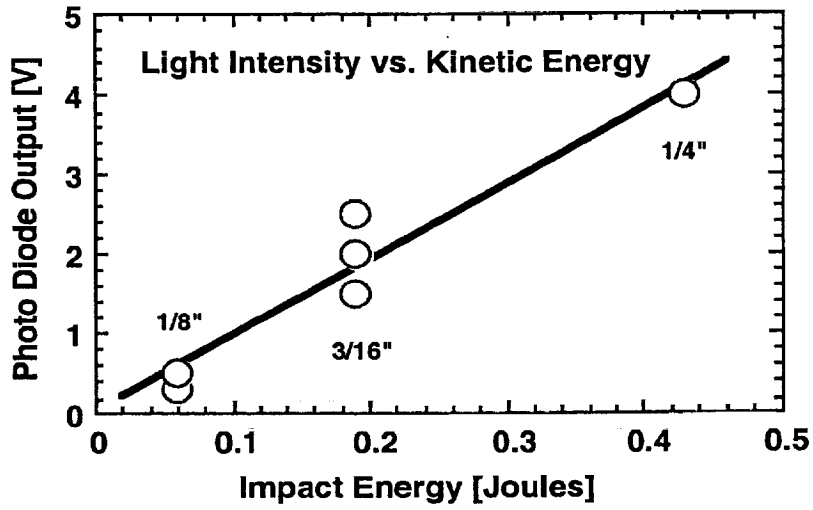

Figure 4: Probable linear relation between the integrated intensity of the delayed light emitted from the rock cores and the kinetic energy of impact.

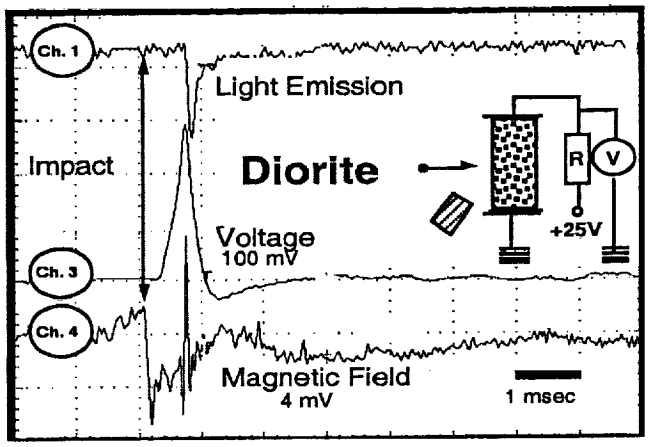

Figure 5. A 100 m/s impact. Cross current measurement with a rectangular piece of diorite impacted at right angle. Channel 1, light emission; channel 3, cross current; channel 4, EM emission (magnetic pick-up coil not shown in inset).

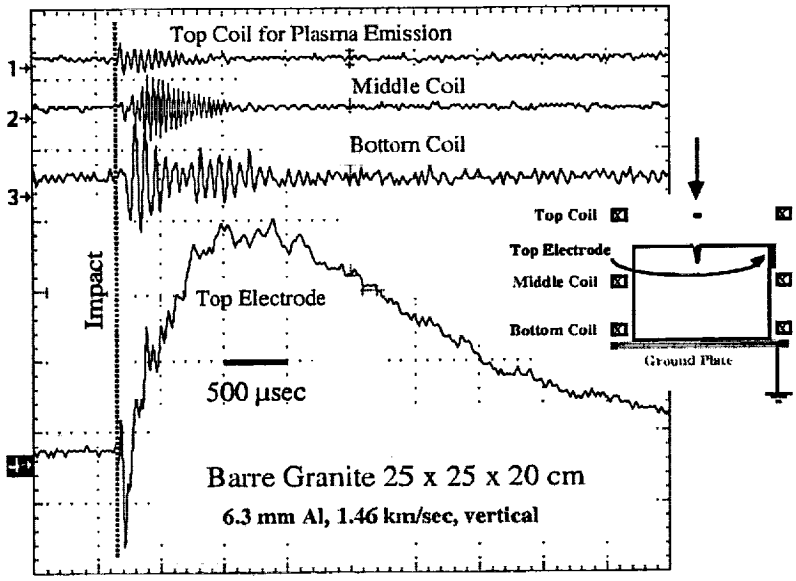

Figure 6. The 1.46 km/s impact of shot 4 on granite with the signals from the three magnetic pick-up coils and the top contact electrode positioned as shown in inset, using the 200-MHz oscilloscope model 420.

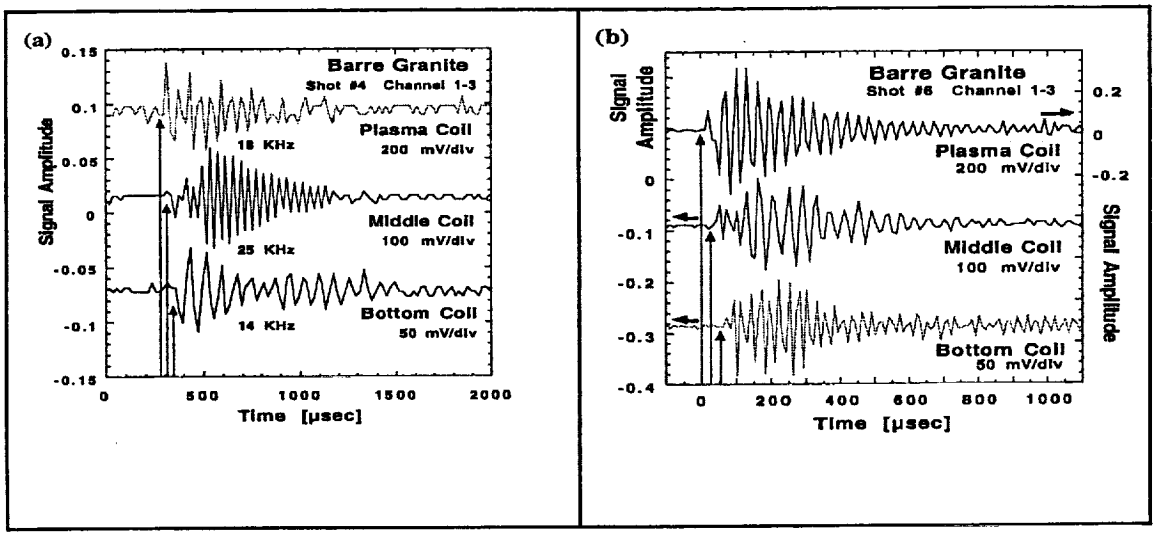

Figure 7. Electromagnetic emission as recorded by the magnetic pick-up coils after impact of the Al sphere (a) during shot 4 at 1.46 km/s, (b) during shot 6 at 4.45 km/s and (c) during shot 7 at 5.64 km/s which led to disintegration of the granite block.

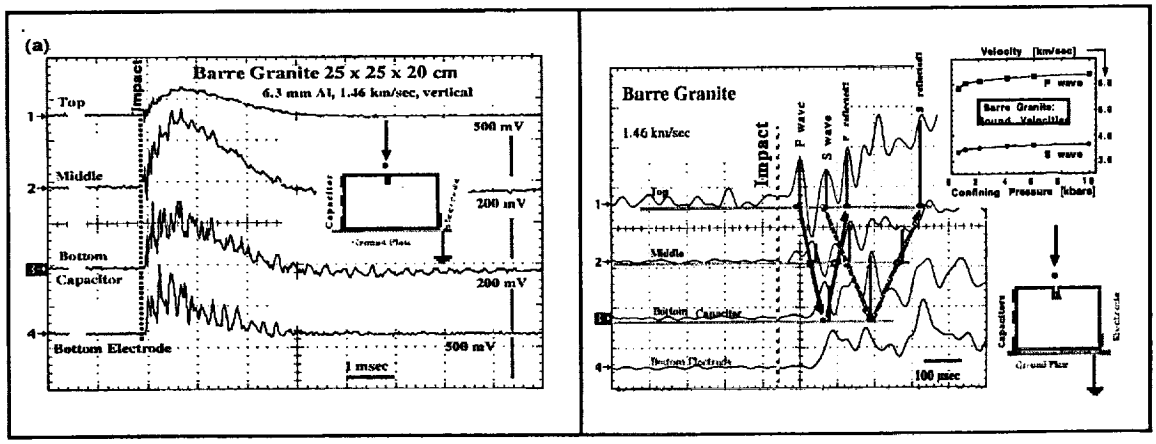

Figure 8. The 1.46 km/s impact of shot 4 on the granite block. (a) Signals from the three capacitive sensors and the bottom contact electrode positioned as shown in the inset, using the 500-MHz oscilloscope model 754. (b) Initial arrival of the signals at higher time resolution with tentative assignment of the short voltage pulses to piezoelectric signals arising from the passing of the incoming and reflected(?) P and S waves. Inset shows velocities of the P and S waves in Barre Granite as a function of the confining pressure after Christensen (1982).

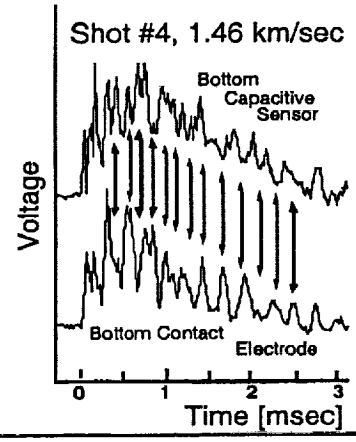

Figure 9.

Out-of-phase correlation between the voltage signal as recorded by the bottom capacitive sensor (top trace) and the electron injection into the rock as recorded by the bottom contact electrode (bottom trace).

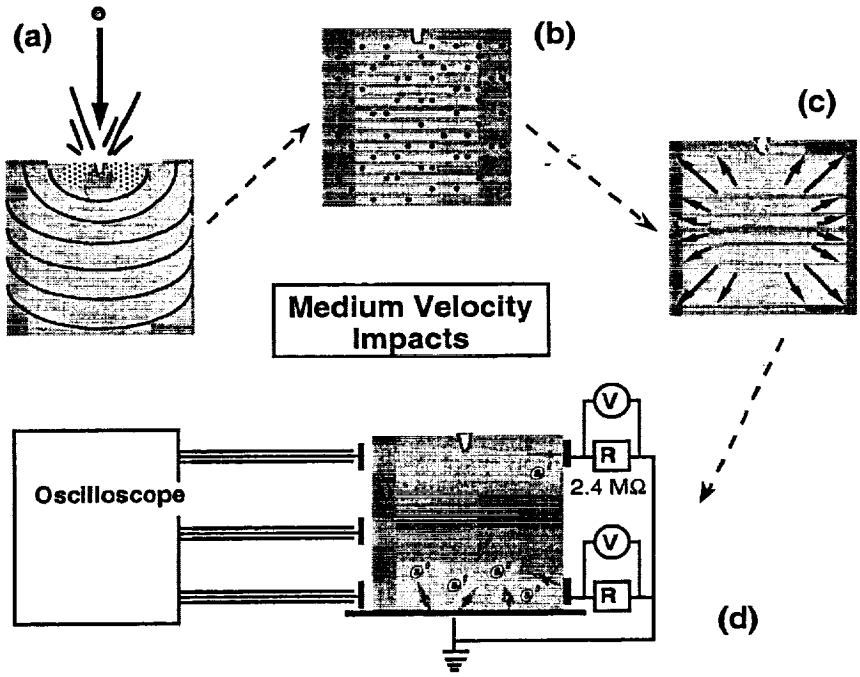

Figure 10. Cartoon of the processes taking place in rapid succession in the granite block following a medium velocity impact. (a) Impact and propagation of the sound waves. (b) Rock volume filled with positive hole charge carriers activated in the wake of the sound waves. (c) Diffusion of positive holes to the surface due to mutual repulsion in the bulk. (d) Injection of electrons from the base plate and contact electrodes leading to oscillations.

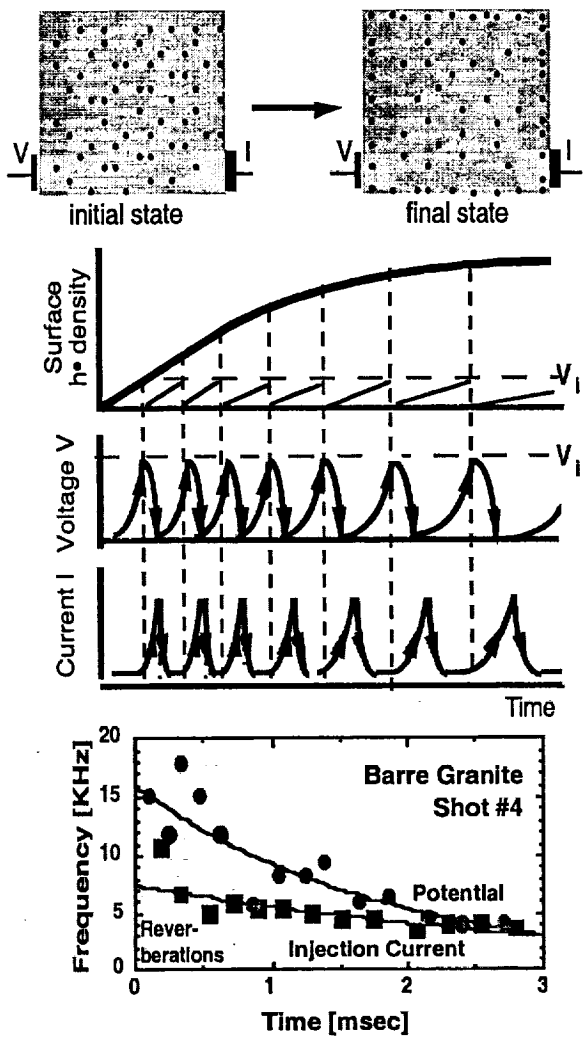

Figure 11. (Top): Cartoon of the transition from the initial state in which the rock volume is uniformly filled with positive hole charge carriers to the final state in which the positive hole charge carriers have redistributed to form a positive surface charge, balanced by a negative interior. The capacitor sensor recording the surface potential V and the contact electrode recording the current I injected in to the rock are indicated. (Middle): Surface charge density as it may develop as a function of time, if the system were unperturbed. (V_i marks the threshold potential at which current injection occurs.) Surface potential V building up repeatedly to the limit of V_I and then breaking down. Pulses of injection current I beginning each time at V_I and breaking down as the surface potential breaks down. (Bottom): Frequency of the surface potential and of the injection current pulses using the data from Figure 9. The time period < 700 μs (shaded) is probably "contaminated" by reverberation of the acoustic waves before they dissipate in the block.

197th Meeting of the American Astronomical Society, 7–11 January 2001—San Diego, CA

Organic Signature of Dust from the Interstellar Medium (ISM)

Friedemann Freund[1], Minoru Freund[2], Aaron Staple[3], and John Scoville[4]

1 SETI Institute/SJSU/NASA Ames
2 NASA GSFC
3 Stanford University
4 University of Kentucky

Abstract

Dust in the ISM carries an "organic" signature in form of a distinct group of $_{CH}$ bands, both in emission and absorption, around 3.4 μm (2800-3000 cm^{-1}). These bands agree with the symmetrical and asymmetrical C–H stretching vibrations of aliphatic $–CH_2–$ entities and are thought to be associated with organic molecules on the surface of dust grains. We show that this interpretation is inconsistent with laboratory experiments. Synthetic MgO and natural olivine single crystals, grown from a $CO/CO_2/H_2O$–saturated melt, exhibit the same $_{CH}$ bands but those bands are clearly associated with C–H entities inside the dense mineral matrix. The multitude of $_{CH}$ bands suggests that the C–H bonds arise from polyatomic C_n entities. We heated the MgO and olivine crystals to temperatures between 550-1000 K to pyrolyze the C–H bonds and to cause the $_{CH}$ bands to disappear. Upon annealing at moderate temperatures between 300-390 K the $_{CH}$ bands reappear within a few days to weeks. The $_{CH}$ intensity increases linearly with the square root of time. Thus, while the pyrolysis broke the C–H bonds and caused the H to disperse in the mineral matrix, the H atoms (or H_2 molecules) are sufficiently mobile to return during annealing and reestablish the C–H bonds. Dust grains that condense in a gas-laden environment (outflow of late-stage stars or in dense molecular clouds) probably incorporate the same type of C_n–H entities. Imbedded in and in part bonded to the surrounding mineral matrix, the C_n–H entities display $_{CH}$ bands in the 3.4 μm region, but their lower frequency librational modes are so strongly coupled to the lattice modes that they broaden excessively and thus become unobservable.

International Association of Geomagnetism and Aeronomy (IAGA) and International Association of Seismology and Physics of the Earth's Interior (IASPEI)—Hanoi, Vietnam, 20-31 August 2001

Earth-Atmospheric Coupling during Strong Earthquakes by Analyzing MODIS Data

Dimitar Ouzounov and Robin G. Williams
NASA Goddard Space Flight Center, Code 902, Greenbelt, MD 20771, USA
Friedemann Freund
NASA Ames Research Center, MS 239-20, Moffett Field, CA 94035-1000, USA

Abstract

Interactions between the Earth and the atmosphere during major earthquakes (M>5) are the subject of this investigation. Recently a mechanism has been proposed [Freund, 2000] predicting the build-up of positive ground potentials prior to strong earthquake activity. Connected phenomena include: transient conductivity of rocks, injection of currents, possibly also electromagnetic emission and light emission from high points at the surface of the Earth. To understand this process we analyze vertical atmospheric profiles, land surface and brightness (temperature) data, using the Moderate Resolution Imaging Spectroradiometer (MODIS) onboard NASA's Terra satellite launched in December 1999. MODIS covers the entire Earth every 1–2 days in 36 wavelength bands (20 visible and 16 infrared) at different spatial resolutions (250 m, 500 m, and 1 km). Using MODIS data we look for correlations between the atmospheric dynamics and solid Earth processes for the January 2001 strong earthquakes in San Salvador and India. As part of the build-up of positive grounds potential, an IR luminescence is predicted to occur in the 8-12 μm band [Geng et al., 1999]. We use the MODIS data to differentiate between true "thermal" signals and IR luminescence. Indeed, on the basis of a temporal and spatial distribution analysis, a thermal anomaly pattern is found that appears to be related to the seismic activity. Aerosol content and atmospheric instability parameters also change when ground charges build up causing ion emission and leading to a thin aerosol layer over land. We analyze the aerosol content, atmospheric pressure, moisture profile and lifted index. Anomalous trends have been identified in few days prior to the main shocks. The significance of this observation should be explored further using other data sets.

Freund, F.: Time-resolved study of charge generation and propagation in igneous rocks, *J. Geophys. Res. 105*, 11001-11019, 2000.

N.Geng, M.Deng, and C.Cui: Simulated experimental studies on earthquake prediction by using infrared and microwave remote sensing, In: *Atmospheric and Ionospheric Electromagnetic Phenomena Associated with Earthquakes*,1999, pp.751-758.

MEPAG-CAPTEM Workshop JPL Aug. 15-16, 2001

SCRATCH 'N SNIFF ON MARS

Friedemann Freund*, J. Thomas Dickinson**, and Ara Chutjian***

* SETI Institute c/o NASA/Ames Research Center, MS 239-20
Moffett Field, CA 94035-1000
650-604-5183(phone)/650-604-1092(fax), e-mail: ffreund@mail.arc.nasa.gov

** Washington State University, e-mail: jtd@wsu.edu

*** Jet Propulsion Laboratory, e-mail: ara.chutjian@jpl.nasa.gov

One of the stated objectives of missions to Mars is to discover whether or not Life ever started on the Red Planet. To achieve this goal, robotic spacecraft and eventually astronauts will survey the rocks in surface environments and in drill boreholes. Instrumentation suitable to achieve these goals have to (1) provide chemical information about the type of rocks encountered, (2) provide information about organics contained therein, (3) provide such information rapidly and with minimum sample preparation or handling.

"Scratch 'n Sniff" is an innovative method (1) to distinguish between magmatic/igneous rocks, sedimentary rocks and salt deposits, and (2) to identify organics in magmatic/igneous minerals. The "Scratch 'n Sniff" sensor combines a diamond stylus with a 16-rod miniature quadrupole mass spectrometer array (QMSA) to analyze atoms and molecules emitted during scratching. The QMSA requires modest vacuum. The stylus is equipped with a strain gauge to simultaneously measure the force applied. Carbonates, chlorides, sulfates, nitrates, and phosphates emit CO/CO_2, Cl_2, SO_x, NO_x, and PO_x, respectively. Hydrous salts emit H_2O. Feldspars emit Na°, K° and Ca. Olivine emits Mg° and Fe°. Igneous minerals in which solute C, H and N have segregated to form $[C\text{-}H\text{-}O\text{-}N]^{n-}$ along dislocations and other defects, emit organic molecules or fragments thereof. The technique is highly sensitive to small concentrations of such proto-organics. The "Scratch 'n Sniff" sensor is compact and of low mass. It will be suitable for deployment on a rover for rapid *in situ* analysis of the mineralogy of the rocks encountered and "sniff" out any organics they may contain. Though the chemical and mineralogical information is only qualitative, the strength of the "Scratch 'n Sniff" sensor is to carry out rapid surveys along Mars transects. If further miniaturized, it may be a candidate for deployment in boreholes.

ABSTRACT

"Scratch 'n Sniff" is an innovative method to recognize magmatic rocks, sedimentary rocks and salt deposits as well as organics, in particular traces of proto-organics in igneous minerals. The "Scratch 'n Sniff" sensor combines a diamond stylus to scratch the surface of a rock with a 16-rod miniature quadrupole mass spectro-meter array (QMSA) to simultaneously analyze atoms and molecules emitted. The stylus is equipped with a strain gauge to measure the force applied. Carbonates, chlorides, sulfates, nitrates, and phosphates emit CO/CO_2, Cl_2, SO_x, NO_x, and PO_x, respectively. Feldspars emit alkali and alkaline earth metal vapors. Olivine emits magnesium and iron metal vapors. Igneous minerals in which solute C, H and N have segregated to form organic protomolecules of the type $[CHON]^{n-}$ along dislocations and other defects, emit organic molecules or fragments thereof. The technique is extremely sensitive to very small concentrations of organics. On a planet with liquid water, rock-bound $[CHON]^{n-}$ represent a potentially large source of complex organics, that would be released by weathering or subsurface hydrothermal leaching.

The "Scratch 'n Sniff" sensor is compact and low mass. We propose to conduct Level One experiments to perfect the "Scratch 'n Sniff" technique and to test it on a wide range of exemplary

minerals and rocks, including meteorites of purported Martian origin, and sedimentary rocks like limestones and shales as well as salt deposits. As a step towards Level Two bread boarding, we propose to integrate a diamond stylus with a miniature QMSA to serve as a testbed under simulated Martian surface conditions. The sensor will be suitable for deployment on a rover to identify in situ and rapidly the composition of rock boulders on Mars and "sniff" whether they contain organics. The "Scratch 'n Sniff" sensor is a candidate for deployment inside boreholes on Mars.

SCIENCE OBJECTIVES AND PROGRAMMATIC RELEVANCE

One of the stated objectives of Astrobiology is to discover whether or not Life ever started on Mars. To achieve this goal, robotic spacecraft and eventually astronauts will be sent to Mars to survey and analyze surface rocks in different environments and to drill boreholes. Instrumentation most suitable to achieve these goals would have to (1) provide information about the type of rocks encountered during rover transects the Martian landscape, (2) provide information about traces of organics contained in these rocks, (3) provide such information rapidly and with minimum sample preparation or handling.

A "Scratch 'n Sniff" sensor proposed here can contribute toward these goals. What no other single technique seems to have been able to offer, the "Scratch 'n Sniff" sensor has the ability to identify rocks and minerals *in situ* and rapidly, as well as detect traces of organics with high sensitivity.

The information obtained will be qualitative, but rapid.

Operation of the "Scratch 'n Sniff" sensor requires contact with the mineral/rock surface. It requires modest vacuum.

Being low mass, small and compact, the sensor will be suitable for rover deployment.

The "Scratch 'n Sniff" sensor has the potential to be miniaturized to a degree that can be deployed inside boreholes.

"SCRATCH 'N SNIFF" EXPERIMENTS

Fracture and abrasion experiments have been performed over several years in Professor Dickinson's laboratory. They have shown that the emission of atomic and molecular species is very similar upon fracture and during abrasion [*Dickinson et al.*, 1987; *Dickinson et al.*, 1986; *Kim et al.*, 1995].

Figure 1 shows the schematic of the laboratory "Scratch 'n Sniff" set-up. It combines on a stylus (attached to a lever arm that carries a strain gauge) with the head of a quadrupole mass spectrometer, and a linear translation stage on which the sample is mounted. As the sample is displaced, the stylus scratches the surface in "fits and bounds", with short periods of rapid motion interlaced with periods where its tip is caught in surface asperities. The background pressure in the laboratory UHV system before scratching is of the order of 10^{-8}-10^{-9} torr. The mass spectrometer may be set to a single mass or to up to four masses in quasi-simultaneous recording or it may be run in a rapid scanning mode, covering the 10-120 amu range in 80 msec.

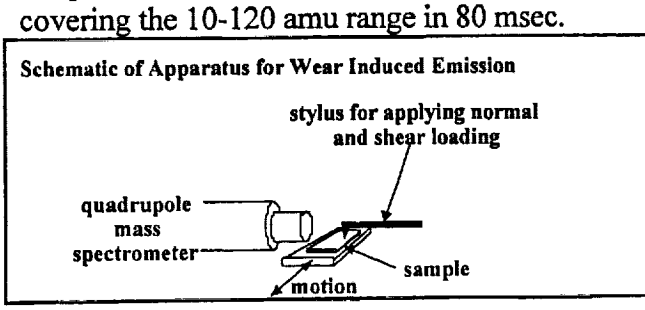

Figure 1:

Schematic of the Scratch N' Sniff experiment to measure the emission of atoms and molecules during abrasion.

MAIN CONSTITUENT OF MINERALS AND ROCKS

Figure 2 (top) shows the 30 amu signal, due to NO^+ from NO that is emitted during the abrasion of single crystal $NaNO_3$ with a stainless steel stylus [*Shin et al.*, 1996].

Figure 2 (center) shows the lateral friction force the between stylus and sample.

Figure 2 (bottom) shows the displacement of the stylus (in mm). NO_2, O_2 and atomic Na emission is observed besides NO.

Figure 3 (top) shows the 44 amu signal, due to CO_2 during 12 strokes of repetitive abrasion of calcite ($CaCO_3$) [*Park et al.*, 1996].

Figure 3 (top) shows how the 44 amu signal evolves during and after a single stroke.

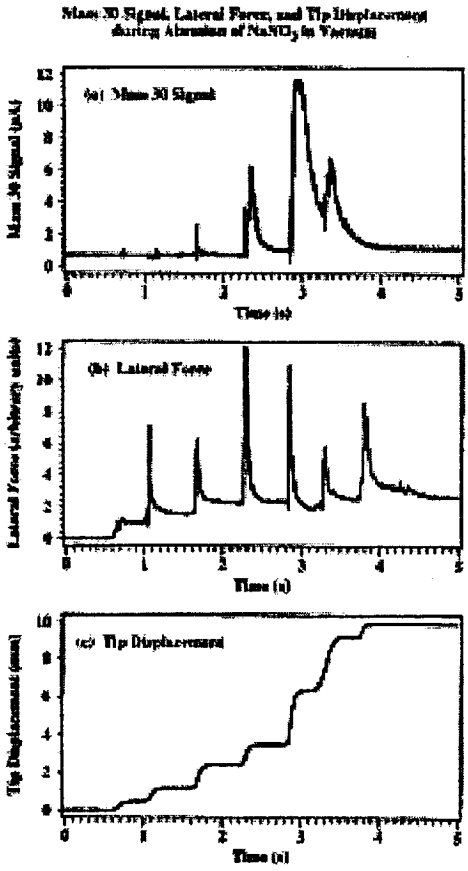

Figure 2: Neutral emission (NO) signals accompanying abrasion of single crystal $NaNO_3$ with accompanying lateral force and stylus displacement measurements (see text).

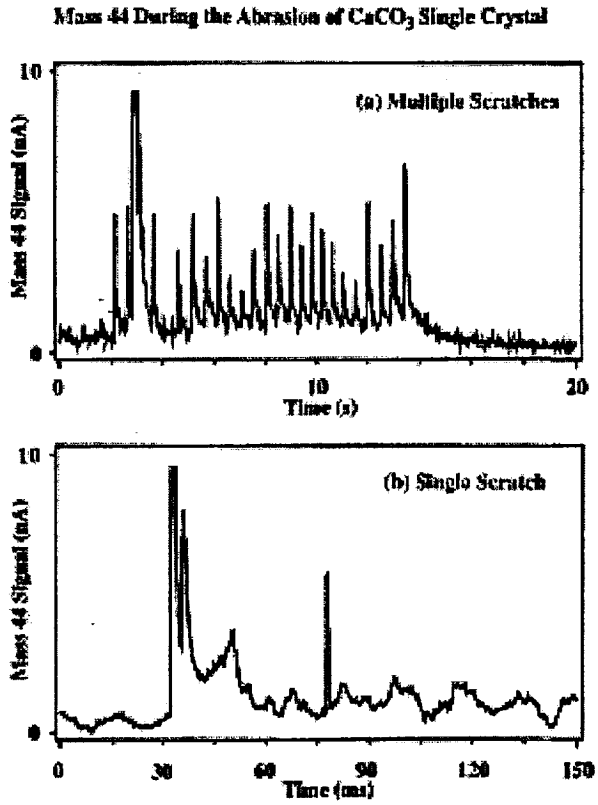

Figure 3: CO_2 emission accompanying the abrasion of single crystal calcite ($CaCO_3$). Top: ~12 reciprocating abrasive strokes; Bottom: a single unidirectional stroke.

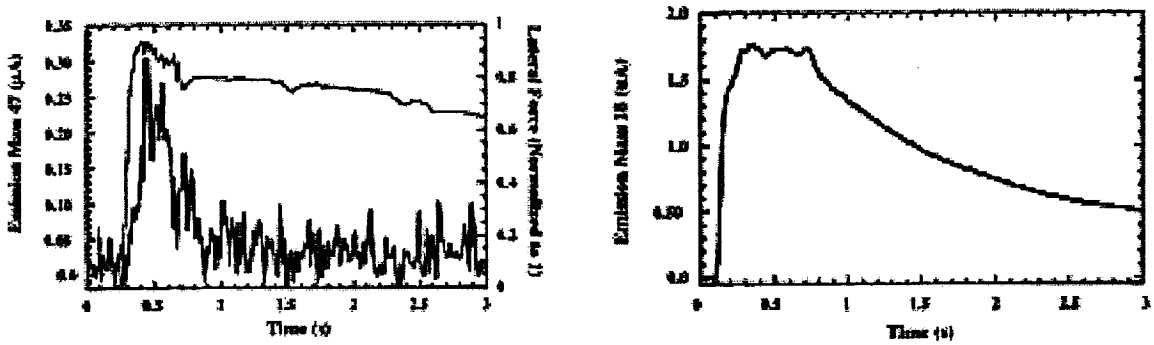

Figure 4. Selected neutral emissions during abrasion of single crystal brushite with diamond. Left: Signal at 47 amu (PO) at an applied load of 3.5 N. Right: Signal at 18 amu (H_2O) detected at an applied load of 2.0 N

Figure 4 (left, bold line to left scale) shows the emission at 47 amu (due to PO^+ from PO) during abrasion of a hydrated phosphate mineral, brushite ($CaHPO_4 \cdot H_2O$).

Figure 4 (left, thin line to right scale) shows the friction force under a 3.5 N load.

Signals were detected simultaneously at 40 amu (Ca^+) and three other anion-derived masses [31 amu (P^+), 32 amu (O_2^+), and 63 amu (PO_2^+).

Figure 4 (right) shows the extremely intense signal at 18 amu (due to H_2O^+ from H_2O) at a normal load of 2 N. The H_2O signal was not only intense, but also lasted for a long time, several seconds, much longer than the decay time of the vacuum, about 100-ms. The persistent H_2O signal probably represents the emission of H_2O molecules diffusing to the surface through cracks. The sensitivity of the abrasion technique to structurally bound water may be helpful in the search for hydrated minerals.

TRACE ORGANIC CONSTITUENT IN IGNEOUS MINERALS

H_2, H_2O, CO, CO_2, plus a wide range of organics are emitted arising from low-z elements that may be contained as "impurities" in the structure of igneous minerals. The enormous enhancement of sensitivity for low-z elements, i.e. the sensitivity for "proto–organics", seems to be one of the hallmarks of the "Scratch 'n Sniff" technique.

SUMMARY

When the stylus scratches across the sample surface, it causes plastic flow, bond breakage and dislocation mobilization. The massive deformation generates electronic charge carriers (electrons and holes) that propagate through the deformed medium and may cause the enhanced emission of organic fragments through electron-stimulated desorption. These processes induced by deformation are similar to those induced by fracture. In both cases, atoms and molecules are emitted that identify the major lattice constituents and any proto-organics that may be contained in the crystal structures.

European Seismological Commission Meeting 2000 Lisbon, Sept. 11-15, 2000 Session SSE-2

"Charge Generation and Propagation in Igneous Rocks"

Friedemann Freund
Physics Department, San Jose State University, and SET Institute, NASA Ames Research Center, Moffett Field; ffreund@mail.arc.nasa.gov

Resistivity changes, ground potentials, electromagnetic (EM) and luminous signals prior to or during earthquakes have been reported, in addition to ground uplift and tilt, and to changes in the seismic wave propagation parameters. However, no physical model exists that ties these diverse phenomena together. Through time-resolved impacts experiments it has been observed that, when igneous rocks (gabbro, diorite, granite) are impacted at low velocities (≈100 m/sec), highly mobile electronic charge carriers are generated, spreading from a small volume near the impact point, causing electric potentials, EM and light emission. The rock becomes momentarily conductive. When impacted at higher velocities (≈1.5 km/sec), the propagation of the P and S waves is registered through the transient piezoelectric response of quartz. At the same time, the rock volume is filled with mobile charge carriers, and a positive surface potential is registered. During the next 1-2 msec the surface potential oscillates, due to electron injection from ground. These observations are consistent with positive holes, e.g. defect electrons in the O^{2-} sublattice, that can travel via the O 2p-dominated valence band of the silicate minerals at the speed of a phonon-mediated charge transfer. Before activation, the positive hole charge carriers lay dormant in form of positive hole pairs, PHP, electrically inactive, chemically equivalent to peroxy links in the structures of constituent minerals. PHPs are introduced by way of hydroxyl (O_3Si-OH) incorporated into nominally anhydrous minerals when they crystallize in water-laden environments. Given that sound waves of even relatively low intensity appear to cause PHPs dissociation, thus generating mobile positive holes, it is proposed that microfracturing during rock deformation cause PHP dissociation. Depending on where and how much the rock volume is stressed, the positive holes are expected to form fluctuating charge clouds in the earthquake source region that may account for earthquake-related electrical phenomena and the reported low frequency EM signals.

PUBLICATIONS DURING YEAR 1:

(i) Freund, F., 2000. Time-resolved study of charge generation and propagation in igneous rocks J. Geophys. Res. 105, 11,001-11,019.

(ii) Freund, F. (1999). "Earthquake Prediction is Worthy of Study." EOS Trans. Amer. Geophys. Soc. **80** 230-232;

(iii) Freund, F., A. Gupta and D. Kumar. (1999). "Carboxylic and dicarboxylic acids extracted from crushed magnesium oxide single crystals." *Origins Life Evol. Biosphere* **29**: 489-509;

(iv) Freund, F. and J. G. Borucki. (1999). "Charge carrier generation and charge cloud propagation following 100m/sec impacts on igneous rocks." in *Atmospheric and Ionospheric Electromagnetic Phenomena Associated with Earthquakes*, M. Hayakawa, ed. Terra Sci. Publ. Tokyo, p. 839-857;

(v) Freund, F., A. Gupta and S. Tenn. (1999). Molecular hydrogen and dormant charge carriers in minerals and rocks. Atmospheric and Ionospheric Electromagnetic Phenomena Associated with Earthquakes." In: *Atmospheric and Ionospheric Electromagnetic Phenomena Associated with Earthquakes*, M. Hayakawa, ed. Terra Sci. Publ. Tokyo, p. 859-871.

OTHER RELEVANT PUBLICATIONS:

(i) Freund, F., and R. Ho, "Organic matter supplied to a planet by tectonic and volcanic activity." In: *Circumstellar Habitable Zones*, ed. L. R. Doyle. (Menlo Park, CA: Travis House, 1996) 71-98.

(ii) Freund, F., Whang, E.-J., Batllo, F., Desgranges, L., Desgranges, C. & Freund, M.M. (1994) "Positive Hole–Type Charge Carriers in Oxide Materials." In: *Grain Boundaries and Interfacial Phenomena in Electronic Ceramics*, Levinson, L.M., ed., Amer. Ceram. Soc. Publ., 263-278

(iii) Freund, F., M. M. Freund & F. Batllo (1993). "Critical review of electrical conductivity measurements and charge distribution analysis of MgO." J. Geophys. Res. 98B, 22,209-229.